

Radiative Transfer Modeling With Biogeochemical-Argo Float Data in the Mediterranean Sea



Key Points:

- Using a multi-spectral radiative transfer model enables to capture the impact of different optically active constituents
- Non-chlorophyll related bio-optical models resulted in better performances compared to chlorophyll-related absorption and scattering models
- Chromophoric dissolved organic matter was the most important optical constituent in the blue, especially at deeper layers

Correspondence to:

E. Terzić,
eterzic@inogs.it

Citation:

Terzić, E., Miró, A., Organelli, E., Kowalczyk, P., D'Ortenzio, F., & Lazzari, P. (2021). Radiative transfer modeling with Biogeochemical-Argo float data in the Mediterranean Sea. *Journal of Geophysical Research: Oceans*, 126, e2021JC017690. <https://doi.org/10.1029/2021JC017690>

Received 16 JUN 2021
Accepted 1 OCT 2021

Elena Terzić¹ , Arnau Miró² , Emanuele Organelli³ , Piotr Kowalczyk⁴ ,
Fabrizio D'Ortenzio⁵ , and Paolo Lazzari¹

¹National Institute of Oceanography and Applied Geophysics—OGS Trieste, Trieste, Italy, ²Barcelona Supercomputing Center (BSC), Barcelona, Spain, ³National Research Council (CNR), Institute of Marine Sciences (ISMAR), Rome, Italy, ⁴Institute of Oceanology Polish Academy of Sciences, Sopot, Poland, ⁵Laboratoire d'Océanographie de Villefranche, Sorbonne Université, CNRS, Villefranche-sur-Mer, France

Abstract A radiative transfer model was parameterized and validated using Biogeochemical Argo float data acquired between 2012 and 2017 across the Mediterranean Sea. Fluorescence-derived chlorophyll *a* concentration, particulate optical backscattering at 700 nm, and fluorescence of chromophoric dissolved organic matter (CDOM) were used to parametrize the light absorption and scattering coefficients of the optically significant water constituents (such as pure water, non-algal particles, CDOM, and phytoplankton). The model was validated with in situ downwelling irradiance profiles and apparent optical properties derived both from irradiance profiles and satellite data, such as the diffuse attenuation coefficients and remote sensing reflectance. Results showed that by using regional parameterizations that are not only related to chlorophyll concentration and vertical distribution, the model was able to capture a more accurate spectral response in the examined wavelength range compared to chlorophyll-related (or Case 1) optical models. When using alternative models that incorporated also measurements of CDOM fluorescence or particulate optical backscattering, the model skill increased at all examined wavelengths. Finally, using a multi-spectral optical configuration also enabled the estimation of the relative contribution of separate water constituents in the examined spectral range. Simulations including non-algal particles and CDOM performed up to 61% and 79% better than when considering the optical properties of pure seawater alone. Moreover, a simulation including phytoplankton light absorption resulted in an error reduction of up to 42%, especially at 412 nm and with a more uniform response at the wavelengths considered.

Plain Language Summary This study integrates numerical simulations (using a multi-spectral optical model) with in situ measurements of floats and remotely sensed observations from satellites. It aims at improving our current understanding of the impact that different constituents (such as pure water, chromophoric dissolved organic matter, detritus, and phytoplankton) have on the in-water light propagation.

1. Introduction

Physical processes in the ocean are fundamentally related to the biogeochemical and light environments and thus impact the growth of phytoplankton, which requires both light and nutrients. In order to get a complete grasp of the complex interaction of physics and biogeochemistry, it is essential to include also numerical models with a physically accurate representation of optics. This in turn enables to quantify with greater precision the impacts of changes in biogeochemical processes (such as primary productivity), circulation patterns (through heat transfer), or the sole nature of absorbing and scattering matter in the examined water body.

Despite this knowledge on the importance of optics, most biogeochemical models, notwithstanding their increasing spatial resolutions, shorter computational times, and improved complexity, still employ an oversimplified methodology for optical calculations, usually to predict photosynthetically available radiation without considering its spectral dependency. One of the few attempts to overcome these limitations have been achieved in Fujii et al. (2007), Dutkiewicz et al. (2015), Mobley et al. (2015), and Gregg and Rousseaux (2016, 2017). In order to improve prediction capabilities on marine biogeochemical features, the

© 2021. The Authors.

This is an open access article under the terms of the [Creative Commons Attribution-NonCommercial-NoDerivs License](https://creativecommons.org/licenses/by/4.0/), which permits use and distribution in any medium, provided the original work is properly cited, the use is non-commercial and no modifications or adaptations are made.

implementation of multi- or hyperspectral optical modeling solutions remains therefore essential, also in order to follow up with the pace of such approaches already adopted in remote sensing and in situ platforms used to successfully observe aquatic biogeochemical phenomena.

With the development of satellites and in situ autonomous platforms, models tend to integrate measurements, either through data assimilation to correct for the numerical drift, or for the validation of the model itself. Combining numerical approaches with experimental data, both from in situ sensors, as well as from satellites, compensates for the shortcomings of each of the separate methods. While model simulations have no spatio-temporal limitations, they are after all numerical representations of natural phenomena that need to be validated accordingly. Satellite remote sensing in the visible range of the spectrum discards more than 90% of the total signal as atmospheric noise, and it is limited to a certain spatial resolution and temporal frequency, reaching only surface layers under clear skies. The emergence of autonomous platforms, such as floats and gliders, can, on the other hand, provide more information also at greater depths, regardless of the sky conditions, and thus surpass the greatest limitations of satellites. Furthermore, they can provide measurements of additional variables that at present cannot be retrieved by satellites. Such sensors are, however, still spatio-temporally heterogeneously distributed and cannot fully replace the synoptic coverage that satellites have.

In order to resolve the distribution of light in the water, information on absorption and scattering properties of the optically significant matter is needed. As such measurements are difficult to obtain, unless field measurements are carried out, semi-empirical relationships between biogeochemical quantities and inherent optical properties (i.e., absorption and scattering spectra) are widely used to facilitate calculations of in-water light propagation. Measurements of biogeochemical quantities, especially phytoplankton chlorophyll *a*, are most widely available, hence the advantage in using them for parameterization purposes.

The Mediterranean Sea has been defined as a bio-optically anomalous region (Bricaud et al., 2002; Corsini et al., 2002; D'Ortenzio et al., 2002; Gitelson et al., 1996; Lee & Hu, 2006; Loisel et al., 2011; Morel, Claustre, et al., 2007; Morel & Gentili, 2009; Organelli, Claustre, et al., 2017; Volpe et al., 2007), so that such global empirical algorithms, both for satellite remote sensing as well as in situ applications, are less accurate. With the adoption of global relationships, Mediterranean waters appeared greener for a given chlorophyll *a* level than waters in other regions (Claustre et al., 2002; Morel & Gentili, 2009).

Among the possible causes for such phenomena could be:

1. Specific phytoplankton community structure (cell size, pigment packaging, pigment composition, and photophysiology), which can affect phytoplankton absorption (a_ϕ) and particle backscattering signals (b_{bp}).
2. Excess of non-algal (mineral) particles (NAP), such as Saharan dust (influencing a_{NAP} and b_{bp}).
3. Excess of chromophoric dissolved organic matter (CDOM), influencing a_{CDOM} ; either separately, or as a combination of several factors (all absorption and scattering coefficients are in units of m^{-1}).

In the past decade, the development of new technologies for the acquisition and analysis of bio-optical variables has brought new insights on CDOM dynamics, size and composition of algal communities, absorption by phytoplankton (a_ϕ), and non-algal particles (a_{NAP}), as well as on particulate backscattering (b_{bp}). Since 2012, a large array of autonomous Biogeochemical Argo (BGC-Argo) floats has been deployed, measuring a whole set of bio-optical and biogeochemical variables (IOCCG, 2011), which could fill the gap between sample acquisitions and remote sensing measurements. With their high vertical resolution profiles, BGC-Argo floats can serve as an additional tool for tackling the bio-optically anomalous nature of the Mediterranean Sea, also due to their high horizontal and vertical spatial coverage (Organelli, Claustre, et al., 2017).

For this reason, an analysis was hereby carried out to show the possibility of using a large array of BGC-Argo float measurements both for a radiative transfer model set-up, as well as for validation purposes. More specifically, profiles of bio-optical and biogeochemical parameters (i.e., fluorescence-derived chlorophyll *a* concentration (Chl), particulate backscattering at 700 nm ($b_{bp}(700)$) and CDOM fluorescence (fDOM)) were used for inherent optical properties (IOP) parameterizations, testing several regionally adopted algorithms for a_ϕ , a_{CDOM} , and a_{NAP} , and particle scattering b_p . Radiometric measurements were, on the other hand, used for model validation.

The aim of this work is to:

1. Test different IOP configurations, especially Chl-versus non-Chl-related bio-optical models.
2. Verify the model performance comparing computation results with BGC-Argo radiometric profiles and apparent optical properties (i.e., diffuse attenuation coefficients for downwelling irradiance and remote sensing reflectances), the latter derived from radiometric profiles and obtained from satellite remote sensing.
3. Check the model sensitivity to different absorption spectra within each group of optically significant constituents (pure water, NAP, CDOM, and phytoplankton)

2. Methods

2.1. BGC-Argo Data Set

The BGC-Argo data set used in this work was obtained from 39 floats operating between 2012 and 2017. The total number of profiles containing Chl measurements was 5,092, however for the sake of the analysis completeness, a few requirements needed to be met. First, only profiles containing the whole suite of following variables were considered: temperature (T , °C), salinity (S , PSU), chlorophyll a (Chl, mgm^{-3}), particle backscattering at 700 nm ($b_{bp}(700)$, m^{-1}), fluorescent component of chromophoric dissolved organic matter (fDOM, ppb of quinine sulfate), and downwelling plane irradiance at 380, 412, and 490 nm ($E_d(\lambda)$, $\mu Wcm^{-2}nm^{-1}$). Profiles lacking at least one of the required variables were excluded from further calculations (2,112). Then, only profiles acquired between 10:00 am and 2:00 pm local time were considered in order to obtain radiometric measurements at low solar zenith angles, thus removing additional 396 profiles. The total number of profiles left for the analysis was 2,584. The quality control (QC) procedure of radiometric data follows the steps described in Organelli, Claustre, et al. (2016), whereas the Chl and $b_{bp}(700)$ QC protocols are found in Schmechtig et al. (2014, 2018). Profiles of all variables were uniformly interpolated on a 1 m grid, starting at 0.5 m. As light is one of the key mechanisms controlling the deep chlorophyll maximum (DCM) depth (Cullen, 2015; Mignot et al., 2014), the choice of the maximum depth range corresponds to the maximum DCM values in the Eastern Mediterranean, which is up to 120 m (Christaki et al., 2001). Therefore, additional 370 profiles were discarded that had depths shallower than 150 m. For a successful calculation of the depth derivative of radiometric profiles the diffuse attenuation coefficients of downwelling irradiance (K_d , m^{-1}) with a non-linear fit of an exponential function with the least squares method, further conditions needed to be met: the first depth measurement of E_d had to be shallower than 1 m (thus discarding 130 profiles) and the number of E_d measurements within the first 10 m had to be at least 5, which discarded another 757 profiles. Moreover, a condition of less than 30% difference between modeled and synthetic E_d (obtained from the K_d at the first optical depth) values was thus added as the existent quality-control procedure for radiometric quantities still retains noisy behavior, which resulted in 147 profiles less. After having applied all the QC procedures, the final number of useful profiles for this work resulted in 1,126, spatially distributed as in Figure 1. In order to remove spikes and negative values, all variables except T and S were further corrected by applying a 5-point median filter, followed by a 7-point running mean. Negative values were assigned to zero. The fact that the applied smoothing procedure might remove some spikes which could be actually indicators of larger aggregates (Briggs et al., 2011), goes beyond the scope of the present study.

2.2. In-Water Radiative Transfer Model

The irradiance distribution along the water column was parameterized into three streams as described in Dutkiewicz et al. (2015) and Gregg and Rousseaux (2016): the direct (E_d^{dir}) and diffuse (E_s) downwelling irradiance components and the upwelling diffuse irradiance (E_u). The downwelling plane irradiance is equivalent to the sum of the two downward streams ($E_d = E_d^{dir} + E_s$). The light spectrum was discretized into 25 nm bands covering the range between 350 and 700 nm. For each band, $E_d^{dir}(\lambda, z)$, $E_s(\lambda, z)$ and $E_u(\lambda, z)$ were solved as a system of three differential equations:

$$\frac{dE_d^{dir}(\lambda, z)}{dz} = -C_d(\lambda, z)E_d^{dir}(\lambda, z), \quad (1)$$

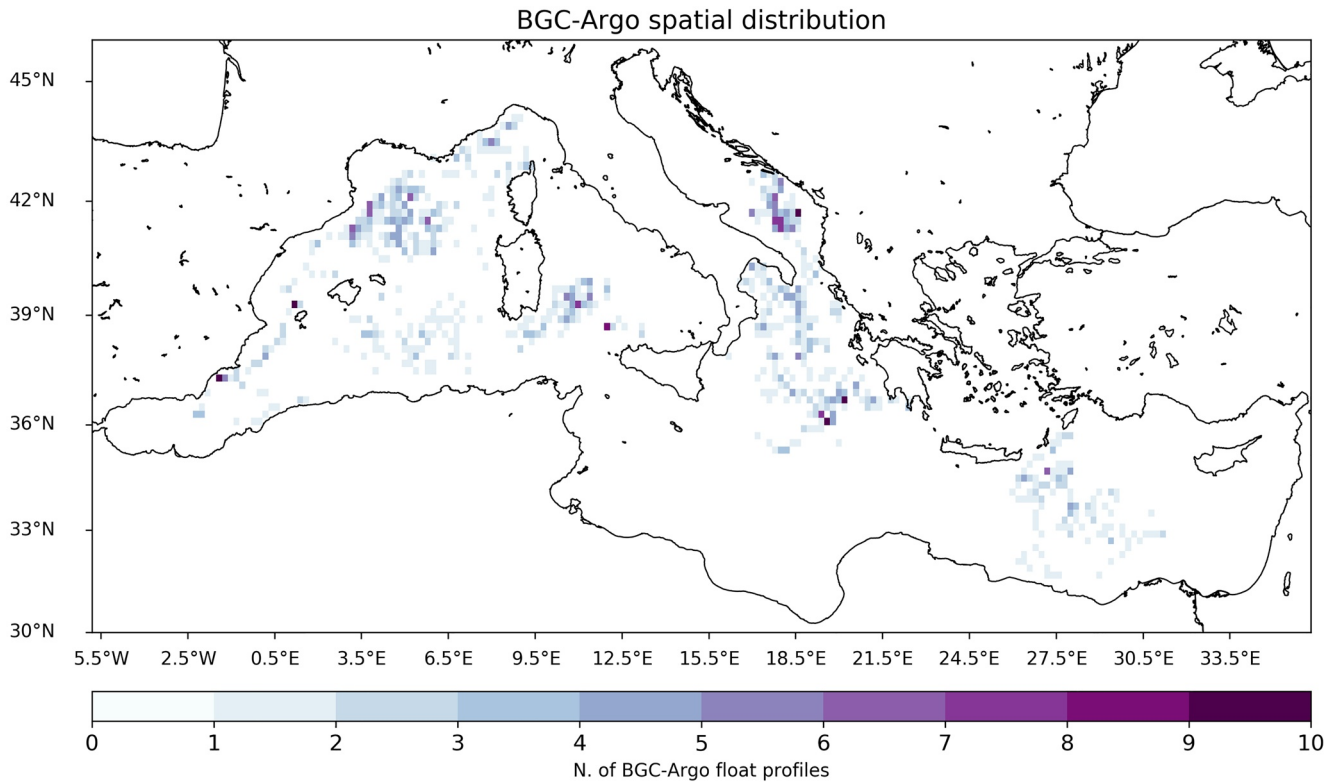


Figure 1. Spatial distribution of the complete data set, after the additional criteria applied to remove profiles which do not meet computation requirements.

$$\frac{dE_s(\lambda, z)}{dz} = -C_s(\lambda, z)E_s(\lambda, z) + B_u(\lambda, z)E_u(\lambda, z) + F_d(\lambda, z)E_d^{dir}(\lambda, z), \quad (2)$$

$$\frac{dE_u(\lambda, z)}{dz} = +C_u(\lambda, z)E_u(\lambda, z) - B_s(\lambda, z)E_s(\lambda, z) - B_d(\lambda, z)E_d^{dir}(\lambda, z), \quad (3)$$

where z is the depth, C_i are the attenuation factors, and B_i and F_d the backward and forward scattering factors, respectively. The attenuation factors C_i were calculated as the sum of absorption (a), scattering (b), and backscattering (b_b) coefficients normalized over cosines:

$$C_d(\lambda, z) = \frac{a(\lambda, z) + b(\lambda, z)}{\mu_d}, \quad (4)$$

$$C_s(\lambda, z) = \frac{a(\lambda, z) + r_s b_b(\lambda, z)}{\mu_s}, \quad (5)$$

$$C_u(\lambda, z) = \frac{a(\lambda, z) + r_u b_b(\lambda, z)}{\mu_u}, \quad (6)$$

In the three-stream approach, the shape factors were considered constant $r_s = 1.5$, $r_u = 3.0$, as well as the average cosines $\mu_s = 0.83$ and $\mu_u = 0.4$ (Aas, 1987), while $\mu_d = \cos(\theta_d^w)$ where θ_d^w denotes the solar zenith angle corrected with water refraction index. Absorption, scattering and backscattering coefficients were defined as a linear combination of separate water constituents:

$$a(\lambda, z) = a_w(\lambda, z) + a_{NAP}(\lambda, z) + a_{CDOM}(\lambda, z) + a_\phi(\lambda, z), \quad (7)$$

$$b(\lambda, z) = b_w(\lambda, z) + b_p(\lambda, z) \quad (8)$$

Different IOP models to determine a , b , and b_b are further presented in Section 2.3.

Scattering factors were similarly defined:

$$B_d(\lambda, z) = \frac{b_b(\lambda, z)}{\mu_d}, \quad (9)$$

$$B_s(\lambda, z) = \frac{r_s b_b(\lambda, z)}{\mu_s}, \quad (10)$$

$$B_u(\lambda, z) = \frac{r_u b_b(\lambda, z)}{\mu_u}, \quad (11)$$

$$F_d(\lambda, z) = \frac{(1 - \tilde{b}_b)b(\lambda, z)}{\mu_d}, \quad (12)$$

where \tilde{b}_b is the ratio of backscattering (b_b) to total scattering (b).

Solving the in-water radiative transfer model requires three boundary conditions, one for each stream. $E_d^{dir}(\lambda, 0^-)$ and $E_s(\lambda, 0^-)$ were derived from the multi-spectral atmospheric radiative transfer model OASIM (Gregg & Casey, 2009), specifically validated with the surface irradiance values from the same BGC-Argo data set in the Mediterranean Sea (Lazzari et al., 2021). The boundary conditions for the upward component were set as $E_u(\lambda, \infty) = 0$. The equations were discretized along depth using the same resolution of the BGC-Argo data and integrated numerically following the methodology described in Dutkiewicz et al. (2015).

2.3. IOP Models

The in-water radiative transfer analysis comprised of six bigger clusters of IOP simulations, as reported below. The aim of these tests was to show that the model does accurately take into consideration the spectral response based on the selection of appropriate IOPs (both absorption and scattering) and thus correctly resolves the radiative transfer equations. By considering one IOP at the time, it was possible to quantify how much does the IOP for a given optically significant constituent contribute to the relative improvement compared to the base. Furthermore, within each constituent, it was possible to assess the impact that each of the model range has at the output at separate wavelengths. In the following subsections, separate groups of IOP models are described in more detail, along with the upgrades that were tested.

1. Pure water absorption and scattering (a_w, b_w).
2. 1. + NAP absorption (a_{NAP}).
3. 1. + CDOM absorption (a_{CDOM}).
4. 1. + phytoplankton absorption (a_ϕ).
5. 1. + particle scattering (b_p).
6. 1. + $a_{NAP} + a_{CDOM} + a_\phi + b_p$

Most models that link biogeochemical quantities with IOPs are assessed for Case 1 water optical types that can be defined as water bodies for which the inherent optical properties (of CDOM and NAP) co-vary with phytoplankton and hence with Chl concentration (Morel & Prieur, 1977). Even though such empirical relationships can be quite useful for parameter estimations, there exists the tendency to oversimplify the optical response of a generally complex biogeochemical environment, as thoroughly discussed in Mobley et al. (2004). Hence, one of the goals of this paper was to try to compare Case 1 water types with alternative parameterizations that considered additional biogeochemical variables and are described in the following subsections.

Simulation results were verified in two different ways. First, modeled irradiance profiles were matched-up with measured E_d profiles at all 3 available wavelengths within the upper 150 m of depth. Second, diffuse attenuation coefficients of downwelling plane irradiances (K_d) for the first optical depth (i.e., the depth range for which the light at a specific wavelength attenuates e-fold) were calculated for both modeled and measured profiles. K_d as an apparent optical property (AOP) does have the advantage of conveying more information on IOPs and to a certain extent remove the impact of the external environment's variability (change in sun location, cloud cover, or surface waves, Mobley et al., 2010). The influence of the external factors is however still present, despite the quality-control procedure introduced by Organelli, Claustre, et al. (2016), resulting in noisy or oddly-shaped profiles which were discarded by including additional

conditions described in Section 2.1. Moreover, at 490 nm it is possible to make a three-platform comparison including model, float and remote sensing data, which is further elucidated in Section 2.4.

2.3.1. Pure Water Absorption and Scattering

The original in-water modeling configuration, described in Gregg and Rousseaux (2016), resolves a pure water absorption spectrum based on data from various sources, as reported therein. However, the UV and blue part of the visible spectrum (from 250 to 550 nm) was improved also with more recent spectrophotometric measurements by Mason et al. (2016), which introduced lower values compared to the findings of Smith and Baker (1981), Morel, Gentili, et al. (2007), Pope and Fry (1997), and Lee et al. (2015). Moreover, pure water absorption was accounted also for the influence on seawater optical properties of T and S according to Sullivan et al. (2006). The original values for pure water scattering from Smith and Baker (1981) and Morel, Claustre, et al. (2007) were further upgraded by calculating values based on the method described by Zhang et al. (2009), thereby accounting for the contribution of T and S. The backscattering-to-total scattering ratio for water is kept as 0.5 as in Gregg and Rousseaux (2016), assuming an isotropic scattering regime.

2.3.2. Non-Algal Particles (NAP) Absorption

The non-algal particles are defined as a composite of living organic particles, such as bacteria, zooplankton, detrital organic matter, and suspended inorganic particles (Mobley et al., 2010). The absorption spectrum, despite its heterogeneous biogeochemical composition, is described with an exponentially decreasing shape from UV to the red part of the spectrum:

$$a_{NAP}(\lambda) = a_{NAP}(\lambda_{ref})e^{-S_{NAP}(\lambda-\lambda_{ref})} \quad (13)$$

The absorption at the reference wavelength, $a_{NAP}(\lambda_{ref})$, can be estimated in two ways: either as a function of Chl (a Case 1 optical water type—see Equation 4 in Bricaud et al., 2010), or by considering the range of values measured in the Mediterranean Sea, that is, between 0.0087 and 0.8 m^{-1} (Babin et al., 2003), with the higher values corresponding to highly turbid waters. The slope S_{NAP} varies from 0.0178 and 0.0104 nm^{-1} , with a mean value of 0.0129 nm^{-1} (Babin et al., 2003). It should be noted, however, that the data collected in the work were from coastal regions, therefore the minimum values could also overestimate the contribution of a_{NAP} compared to the open ocean. To better reproduce the vertical distribution of NAP, different profile shapes are considered when estimating model IOPs: Case 1 optical types assume a co-variability with Chl, and additional tests were performed by considering $b_{bp}(700)$ as a better proxy for non-algal particle vertical distribution.

The b_{bp} signal is comprised both of organic and inorganic particles, however, the separation of the two fractions is at present still not possible to achieve. As it has already been demonstrated that the contribution of detrital non-algal particles to the total b_{bp} signal can be very high in Mediterranean waters (Bellacicco et al., 2019), a hypothesis was placed to consider $b_{bp}(700)$ as a better parameter than Chl from the BGC-Argo set of measurements in terms of NAP depth variability. The summary of a_{NAP} models is shown in Table 1.

2.3.3. CDOM Absorption

Similarly to a_{NAP} , the spectral response of a_{CDOM} is also parameterized with a decreasing exponential function:

$$a_{CDOM}(\lambda) = a_{CDOM}(\lambda_{ref})e^{-S_{CDOM}(\lambda-\lambda_{ref})} \quad (14)$$

$a_{CDOM}(\lambda_{ref})$ can be also estimated as a function of Chl from a regional Case 1 model presented in Morel and Gentili (2009) which is based on spectral coefficients of pure water as measured by Pope and Fry (1997). However, given the substantial modification of the a_w absorption spectra in the UV/blue range when following Mason et al. (2016) compared to originally adopted values from Pope and Fry (1997), a set of simulations was tested by subtracting the former $a_{ORIG}(\lambda)$ with the updated one, a_w , as shown in Equation 15. With previous values, $a_w^{ORIG}(\lambda)$ amounted to a higher water absorption, which would have led to a significant underestimation of a_{CDOM} .

$$a_{CDOM}^{corr}(\lambda) = a_{CDOM}(\lambda) + a_w^{ORIG}(\lambda) - a_w(\lambda) \quad (15)$$

Table 1
List of All the Models Used in This Study

a_{NAP}						
Name	Model	Equation	Profile shape	S_{NAP} range	a_{NAP} (443) range	
$a_{NAP_Case1_Chl}$	Bricaud et al. (2010)	$0.013Chl^{0.615} e^{-S_{NAP}(\lambda-440)}$	Chl	0.0104–0.0178	-	
$a_{NAP_Case1_b_{bp}}$			$b_{bp}(700)$			
$a_{NAP_Babin_Chl}$	Babin et al. (2003)	$a_{NAP}(443)e^{-S_{NAP}(\lambda-443)}$	Chl	0.0104–0.0178	0.0087–0.8	
$a_{NAP_Babin_b_{bp}}$			$b_{bp}(700)$			
Final	Babin et al. (2003)	$a_{NAP}(443)e^{-S_{NAP}(\lambda-443)}$	$b_{bp}(700)$	0.0129	0.0087	
a_{CDOM}						
Name	Model	Equation	Profile Shape	S_{CDOM} range		
$a_{CDOM_Case1_Chl}$	Morel and Gentili (2009)	$0.0316Chl^{0.63} e^{-S_{CDOM}(\lambda-443)}$	Chl	0.015–0.02		
$a_{CDOM_Case1_fDOM}$			fDOM			
$a_{CDOM_K_{bio_Morel}}$	$a_{CDOM}(380) \equiv K_{bio}(380)$	$a_{CDOM}(380)e^{-S_{CDOM}(\lambda-380)}$	fDOM	0.015–0.02		
$a_{CDOM_K_{bio_Mason}}$						
$a_{CDOM_K_{bio_Mason_a_w_corr}}$						
Final	$a_{CDOM}(380) \equiv K_{bio}(380)$	$a_{CDOM}(380)e^{-S_{CDOM}(\lambda-380)}$	fDOM	0.017		
b_p						
Name	Model	$b_p(\lambda)$	$b_{bp}(\lambda)$	Profile Shape	$\widetilde{b_{bp}}$ range	η range
$b_{p_Case1_Chl}$	Morel et al. (2002)	$0.416Chl(z)^{0.766} \frac{\lambda}{550}^v$	$\widetilde{b_{bp}} b_p(\lambda)$	Chl	0.002–0.015	0–4
$b_{p_Case1_b_{bp}}$				$b_{bp}(700)$		
$b_{p_from_b_{bp}}$	Antoine et al. (2011)	$\frac{\widetilde{b_{bp}}(\lambda)}{b_{bp}}$	$b_{bp}(700) \left(\frac{\lambda}{700} \right)^{-\eta}$	$b_{bp}(700)$	0.002–0.015	0–4
Final	Antoine et al. (2011)	$\frac{\widetilde{b_{bp}}(\lambda)}{b_{bp}}$	$b_{bp}(700) \left(\frac{\lambda}{700} \right)^{-\eta}$	$b_{bp}(700)$	0.015	3

Note. Either Case 1 from Bricaud et al. (2010) for a_{NAP} , Morel & Gentili (2009) for a_{CDOM} and Morel et al. (2002) for b_p or the non-Case 1 from Babin et al. (2003) for a_{NAP} , Organelli & Claustre (2019) for a_{CDOM} where $a_{CDOM}(380) \equiv K_{bio}(380)$ and Antoine et al. (2011) for b_p . The profile shape follows either Chl, $b_{bp}(700)$ or fDOM, with different ranges of the model parameters for each IOP: S_{NAP} , $a_{NAP}(443)$, S_{CDOM} , $\widetilde{b_{bp}}$ and η .

The remaining parameter to estimate was the slope S_{CDOM} , which can be taken from Babin et al. (2003) and Organelli et al. (2014), that is, ranging between 0.015 and 0.02 nm^{-1} , with a mean value of 0.017 nm^{-1} . As with NAP, the Case 1 model for a_{CDOM} was upgraded by considering the fDOM profile shape instead of a vertical parameterization depending only on Chl. Following Organelli and Claustre (2019), $a_{CDOM}(380)$ was approximated with $K_{bio}(380)$, which was in turn calculated from the diffuse attenuation coefficient $K_d(380)$. The latter was derived from the BGC-Argo irradiance profiles at 380 nm, both for the mixed layer as for the first optical depth. The former was obtained from a potential density threshold value criterion (de Boyer Montégut et al., 2004), whereas the latter corresponds to the e-folding depth at the specific wavelength. $K_d(380)$ was then estimated from a non-linear fit with the least squares minimization of an exponential function for both depth ranges, and can be separated into pure water and biogenic components (Morel & Maritorena, 2001):

$$K_d(\lambda) = K_w(\lambda) + K_{bio}(\lambda), \quad (16)$$

where:

$$K_w(\lambda) = a_w(\lambda) + 0.5b_w(\lambda) \quad (17)$$

After having subtracted the pure water contribution $K_w(380)$ as estimated in Morel and Maritorena (2001) (i.e., 0.0151 m^{-1}), the remaining item, $K_{bio}(380)$, serves as a proxy for $a_{CDOM}(380)$. As discussed in Organelli and Claustre (2019), there are several previous studies in the clearest oligotrophic world oceans that have shown that CDOM dominates the light absorption budget at 380 nm (see references therein). a_{NAP} at 380 nm contributes less than 20% to total non-water absorption in clear oligotrophic waters (Bricaud et al., 2010).

In the absence of coincident light absorption data to prove that these conclusions hold true also in the present case, other possible sources that affect light attenuation in the UVs, such as light absorption by mycosporine-like amino acids and NAP, might be excluded or considered negligible. Instead, an additional set of simulations was performed by changing the relative contribution of K_{bio} (380) by assigning a factor f ranging between 0.5 and 1. In this way, different relative contributions of other constituents could be assessed while leaving some uncertainty in the method to use K_{bio} (380) as a proxy for a_{CDOM} only.

Given the fact that the IOP models used here for pure water absorption are the new measurements of Mason et al. (2016), and a T - S correction is applied (Sullivan et al., 2006; Zhang et al., 2009), different tests were tried in order to calculate K_w (380) as a function of a_w (380) and b_w (380) rather than adopting a constant value. The entire a_{CDOM} spectrum is then estimated with the slope range of values as described above, with the depth variability analogous to the fDOM shape. The summary of a_{CDOM} models is shown in Table 1.

2.3.4. Phytoplankton Absorption

For phytoplankton Chl-specific absorption spectra, data for seven different algal species of varying size were used, with organisms adequate for surface applications, and several strains suitable for both surface and mixed layer (more details in Organelli, Nuccio, et al., 2017). Absorption spectra were obtained for species cultured at the light regime of 100 μmol photons $\text{m}^{-2}\text{s}^{-1}$.

The total phytoplankton absorption is computed as the sum of separate phytoplankton functional types (PFT) spectra $a_{\phi}^i(\lambda)$ as shown in Equation 18:

$$a_{\phi}(\lambda, z) = \sum_{i=1}^6 a_{\phi}^i(\lambda) f_{\phi}^i \text{Chl}(z), \quad (18)$$

The relative contribution of each PFT to the total Chl concentration, $f_{\phi}^i(z)$, followed the regional empirical algorithm introduced by Di Cicco et al. (2017, Table 4). For that purpose, seven algal species were merged into six PFTs: *Diatoms*, *Dinoflagellates*, *Cryptophytes*, *Green Algae* and *Prochlorococcus*, *Prochlorococcus* and *Synechococcus*, *Coccolithophores*. The relative contribution of *Prochlorococcus* was divided into 0.5 for the 2 PFTs containing the same species. Original spectra with a 1 nm frequency were converted to 25 nm bins, corresponding to the model spectral resolution.

The regional algorithm of Di Cicco et al. (2017) was validated with in situ data for first 50 m, with the majority of samples in the Western Mediterranean. Apart from the spatio-temporal bias inherent to ship-borne measurements with which the relationship was obtained, it is suitable for Chl values in the range between 0.02 and 5.52 mgm^{-3} . Therefore, Chl values higher than 5.52 mgm^{-3} or lower than 0.02 mgm^{-3} have been limited to Chl = 5.52 and 0.02 mgm^{-3} , respectively. The lower limit was placed in order to avoid numerical instabilities, whereas the higher limit was reached in only 5 profiles out of 1,126, all of them present in the North-Western Mediterranean during spring blooms (i.e., 5.71, 5.77, 5.82, 5.96, 5.53 mgm^{-3}). No special features were observed in any of the limiting cases.

2.3.5. Particle Scattering

Unlike the model set-up in Gregg and Rousseaux (2016), the particle scattering b_p is resolved as a total sum, and not partitioned into the relative scattering contributions of separate PFTs plus NAP. Following Equation 14 in Morel et al. (2002), b_p is expressed as a function of Chl:

$$b_p(\lambda, z) = 0.416[\text{Chl}(z)]^{0.766} \left(\frac{\lambda}{550} \right)^{\nu}, \quad (19)$$

where $\nu = 0.5[\log_{10}(\text{Chl}) - 0.3]$ if $0.02 < \text{Chl} < 2\text{mgm}^{-3}$ and $\nu = 0$ if $\text{Chl} > 2\text{mgm}^{-3}$. ν values are between -1 and 0 . Commonly used in earlier models, the value of $\nu = -1$ is derived from Mie theory and is known to be valid only for non-absorbing particles with a Junge particle size distribution slope of -4 (Van de Hulst, 1981) with a particle size range between $D_{\min} = 0$ and $D_{\max} = \infty$ (Boss et al., 2001). Similarly to the PFT regional algorithm modification, ν is calculated as if Chl were equal to 0.02 mgm^{-3} for values lower than the minimum concentration. Both Chl and b_{bp} (700) vertical profiles were taken into consideration to account for the depth variability. Alternatively, b_{bp} (700) from BGC-Argo floats can be also used to estimate b_p . A spectrum of $b_{bp}(\lambda)$ can be obtained from Equation 20:

$$b_{bp}(\lambda) = b_{bp}(\lambda_o) \left(\frac{\lambda}{\lambda_o} \right)^{-\eta}, \quad (20)$$

where η describes the backscattering spectral slope and can be related to particle size distributions, assuming that the particles are non-absorbing. Lower slope values (around 0–1) indicate the presence of larger particles and vice-versa. The range of tested values was between 0 and 4, where the highest slope value agrees with measurements at the BOUSSOLE buoy (Antoine et al., 2011), and a mean value of 2 was found according to Organelli, Bricaud, et al. (2016). The relative contribution of back-to total particle scattering can be quantified with a known backscattering ratio \widetilde{b}_{bp} :

$$\widetilde{b}_{bp} = \frac{b_{bp}(\lambda)}{b_p(\lambda)}, \quad (21)$$

in the present set of simulations ranging between 0.002 and 0.015 and spectrally constant (Antoine et al., 2011). The depth variability follows $b_{bp}(700)$ profiles.

2.4. Remote Sensing Data

Both AOPs, that is, remote sensing reflectance and K_d , can be described as functions of absorption and (back)scattering coefficients (Gordon, 1989; Morel & Gentili, 1993).

In order to compare model data with satellite measurements, the calculation of in-water remote sensing reflectance $R_{rs}^-(\lambda)$ from the model was carried out by following:

$$R_{rs}^-(\theta_o, \lambda, Chl) = \frac{Eu(\lambda)}{Ed(\lambda)} \frac{1}{Q(\theta_o, \lambda, Chl)}, \quad (22)$$

where the calculation of Q , a function of wavelength λ , Chl, and solar zenith angle θ_o , follows the procedure introduced by Morel et al. (2002):

$$Q(\theta_o, \lambda, Chl) = Q_o(\theta_o, \lambda, Chl) + S_{Qn}(\lambda, Chl)[1 - \cos(\theta_o)] \quad (23)$$

Values of $Q_o(0, \lambda, Chl)$ and $S_{Qn}(0, \lambda, Chl)$ are interpolated from the look-up Table 2 in the Case 1 model from Morel et al. (2002). Surface Chl values were taken from float measurements at the shallowest depth. In case of Chl concentrations below 0.03 mgm^{-3} , $Q_o(0, \lambda, Chl)$ and $S_{Qn}(0, \lambda, Chl)$ were taken from the minimum value.

The conversion from in-water to above-water remote sensing reflectance R_{rs}^+ (hereafter R_{rs}) follows the relationship from Lee et al. (2002):

$$R_{rs} = \frac{0.52R_{rs}^-}{1 - 1.7R_{rs}^-} \quad (24)$$

Satellite data were obtained from Copernicus Marine Environment Monitoring Service the Ocean Color Level 3 products (OCEANCOLOUR MED OPTICS L3 REP OBSERVATIONS 009 095), comprising of $R_{rs}(\lambda)$ data at 6 wavelengths: 412, 443, 490, 510, 555, 670 nm, as well as of the diffuse attenuation of downwelling irradiance at 490 nm, $K_d(490)$. Given the fact that no upwelling component of irradiance measurements E_u is available from BGC-Argo floats, a more in-depth study of most appropriate scattering regimes is left for similar tests with data from multi-spectral platforms as ProVal (Leymarie et al., 2018)

Locations of floats were matched-up with daily satellite data of a 1 km grid space resolution. A total of 445 points were left for the period corresponding to the simulations considered. Due to a reduced number of matched-up quantities, the values of $R_{rs}(\lambda)$ and $K_d(490)$ were spatially averaged to Western and Eastern Mediterranean basins, and temporally in the form of monthly climatological values.

3. Results and Discussion

3.1. IOP Model Validation

In order to verify the improvement of various modeling configurations, simulations were clustered into groups of separate IOPs, each with its own selection of tests and modifications. The model skill was quantified with three statistical parameters (root mean square error or RMSE, bias, and Pearson correlation coefficient r), resulting from a point-by-point match-up of modeled and measured downwelling irradiance values for the first 150 m at three wavelengths.

Table 2

Summary of the Skill of Simulations (Only Pure Water IOPs, Pure Water IOPs and a_{NAP} , Pure Water IOPs and a_{CDOM} , and Pure Water IOPs Plus Separate IOPs) Quantified in Terms of Relative Changes in Root Mean Square Error ($\Delta RMSE$), Bias ($\Delta bias$), and Pearson Correlation Coefficient (Δr) With Respect to the Previous Model Configuration (i.e., One Line Above in the Table)

Name	Model	Profile shape	Metrics								
			380 nm			412 nm			490 nm		
			$\Delta RMSE[\%]$	$\Delta bias[\%]$	$\Delta r[\%]$	$\Delta RMSE[\%]$	$\Delta bias[\%]$	$\Delta r[\%]$	$\Delta RMSE[\%]$	$\Delta bias[\%]$	$\Delta r[\%]$
Pure water											
a_w _Gregg	Gregg and Rousseaux (2016)	-	-	-	-	-	-	-	-	-	-
a_w _Mason	Mason et al. (2016)	-	40.6	40.0	-41.0	22.0	22.2	-15.0	-	6.7	-
a_w _Mason_TS	Mason et al. (2016) T-S corrected	-	-5.0	-5.0	11.4	-14.0	-14.0	15.8	-5.0	-	-
Final	relative to the initial configuration	-	34.4	33.0	-32.4	5.0	6.0	-2.5	-5.0	6.7	-
Pure water IOPs and a_{NAP}											
a_{NAP} _Case1_Ch1	Bricaud et al. (2010)	Ch1	-	-	-	-	-	-	-	-	-
a_{NAP} _Case1_ b_{bp}	Bricaud et al. (2010)	b_{bp} (700)	-12.5	-11.2	11.2	-10.0	-7.5	4.0	-	-7.2	-
a_{NAP} _Babin_Ch1	Babin et al. (2003)	Ch1	-	-4.2	-2.9	-3.4	-8.0	-1.3	-	-	-1.1
a_{NAP} _Babin_ b_{bp}	Babin et al. (2003)	b_{bp} (700)	-40.0	-39.2	22.4	-31.0	-34.8	9.1	-10.6	-15.4	1.10
Final	relative to the initial configuration	b_{bp} (700)	-47.0	-49.2	32.2	-39.4	-44.5	12.0	-10.6	-21.5	-
Pure water IOPs plus a_{CDOM}											
a_w _Mason_TS	Mason et al. (2016)	-	-	-	-	-	-	-	-	-	-
a_{NAP} _Babin_ b_{bp}	Babin et al. (2003)	b_{bp} (700)	-60.5	-65.0	86.4	-53.5	-60.5	27.3	-19.0	-31.2	2.2
a_{CDOM} _K _{bio} _Mason_ a_w _corr	Organelli and Claustre (2019)	fDOM	-79.1	-87.5	102.0	-72.1	-84.2	36.4	-33.3	-50.0	4.5
a_ϕ	Di Cicco et al. (2017)	Ch1	-32.6	-37.5	52.3	-41.9	-50.	22.7	-28.6	-43.8	4.5
b_p	Antoine et al. (2011)	b_{bp} (700)	-4.7	-5.0	11.4	-11.6	-13.2	9.1	-19.0	-31.3	2.2
Pure water IOPs plus separate IOPs: a_{NAP}, a_{CDOM}, a_ϕ and b_p											
a_w _Mason_TS	Mason et al. (2016)	-	-	-	-	-	-	-	-	-	-
a_{NAP} _Babin_ b_{bp}	Babin et al. (2003)	b_{bp} (700)	-60.5	-65.0	86.4	-53.5	-60.5	27.3	-19.0	-31.2	2.2
a_{CDOM} _K _{bio} _Mason_ a_w _corr	Organelli and Claustre (2019)	fDOM	-79.1	-87.5	102.0	-72.1	-84.2	36.4	-33.3	-50.0	4.5
a_ϕ	Di Cicco et al. (2017)	Ch1	-32.6	-37.5	52.3	-41.9	-50.	22.7	-28.6	-43.8	4.5
b_p	Antoine et al. (2011)	b_{bp} (700)	-4.7	-5.0	11.4	-11.6	-13.2	9.1	-19.0	-31.3	2.2

Starting with a pure water IOP model, the updated absorption spectrum in the UV/blue range (a_w _Mason, Mason et al., 2016) reveals a skill deterioration due to a much lower water absorption in the tested range of the spectrum. Most noticeably at shorter wavelengths, RMSE increases by 0.13, 0.09, and 0.01 $Wm^{-2}nm^{-1}$ (40.6%, 22%, and < 1%) at 380, 412, and 490 nm, respectively, compared to the “reference” simulation (a_w _Gregg, with the pure water absorption spectrum used in Gregg & Rousseaux, 2016). Similarly, bias increases by 0.12, 0.08, and 0.01 $Wm^{-2}nm^{-1}$ (40%, 22.2%, and 6.7%) compared to the reference configuration. The correlation coefficient r decreases by 0.26, 0.10, and 0.001 (41%, 15%, and < 1%), respectively, Figure 2a and Table 2. a_w values from Mason et al. (2016) are chosen as reference in subsequent simulations, assuming that the latest technology development enabled more accurate spectral measurements.

The inclusion of T and S data both for absorption (Sullivan et al., 2006) and scattering spectra (Zhang et al., 2009) displays a smaller, however notable improvement in the model’s skill. Compared to the simulation with absorption values from Mason et al. (2016), RMSE decreases by 0.02, 0.07, and 0.01 $Wm^{-2}nm^{-1}$ (5%, 14%, and 5%) and the bias by 0.02, 0.06, and < 0.01 $Wm^{-2}nm^{-1}$ (5%, 14%, and < 1%). The last configuration (a_w _Mason_TS), with the modification from Mason et al. (2016) and T-S corrected models of a_w and b_w , was therefore chosen for subsequent tests.

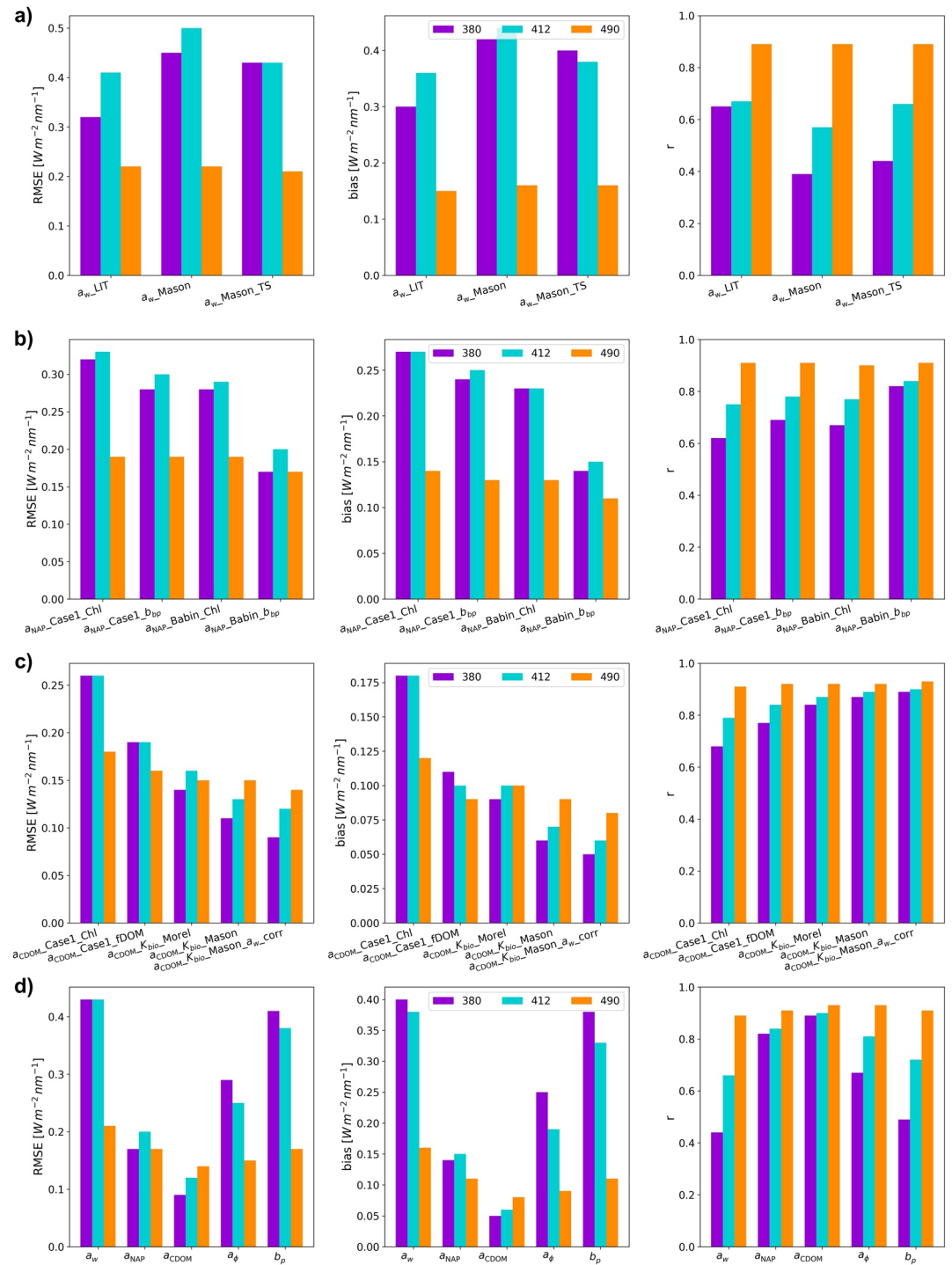


Figure 2. Bar plots resulting from a point-by-point match-up with modeled and measured E_d values. The three figures (from left to right) show bias, root mean square error, and Pearson correlation coefficient, respectively. Each simulation type has three bar plots, representing different wavelengths (purple: 380 nm, cyan: 412 nm, and dark blue: 490 nm): (a) Pure water IOPs. (b) Pure water IOPs and a_{NAP} . (c) Pure water IOPs and a_{CDOM} . (d) Pure water plus separate IOPs: a_{NAP} , a_{CDOM} , a_ϕ , and b_p .

A series of tests were performed for a_{NAP} parameterizations, Figure 2b and Table 2. Starting with a Case 1 model that follows the Chl profile shape ($a_{NAP_Case1_Chl}$), the consecutive improvements incorporated the inclusion of $b_{bp}(700)$ depth variability ($a_{NAP_Case1_b_{bp}}$). Moreover, the range of $a_{NAP}(443)$ and S_{NAP} values from Babin et al. (2003) were tested with both Chl and $b_{bp}(700)$ shapes ($a_{NAP_Babin_Chl}$ and $a_{NAP_Babin_b_{bp}}$). Among the tests with a varying range of values (S_{NAP} between 0.0104 and 0.0178, and $a_{NAP}(443)$ between 0.0087 and $0.08\ m^{-1}$, the latter corresponding to highly turbid waters), the minimum value for $a_{NAP}(443)$ was chosen, assuming that floats are located in open waters with a low or negligible contribution of sediments. The slope S_{NAP} is selected from a mean value of 0.0129 from Babin et al., 2003.

Considering $b_{bp}(700)$ vertical profile ($a_{NAP_Case1_b_{bp}}$) instead of Chl ($a_{NAP_Case1_Chl}$) in the Case 1 configuration from Bricaud et al. (2010) significantly increases the skill, especially toward the UV, as the RMSE decreases by 0.04, 0.03, and $0.001\ Wm^{-2}\ nm^{-1}$ (12.5%, 10%, and less than 1%). The bias, on the other hand, decreases by 0.03, 0.02, and $0.01\ Wm^{-2}\ nm^{-1}$ (11.2%, 7.5%, and 7.2%). Shifting toward non-Case-1 representations, with the inclusion of the range of values observed in in situ measurements, gives an overall better match-up statistics, which especially improves when considering the $b_{bp}(700)$ vertical profile ($a_{NAP_Babin_b_{bp}}$), Figure 2b. Comparing the $b_{bp}(700)$ -shaped model with values from Babin et al. (2003) ($a_{NAP_Babin_b_{bp}}$) and the analogous Case 1 model ($a_{NAP_Case1_b_{bp}}$), RMSE decreases by 0.11, 0.11, $0.02\ Wm^{-2}\ nm^{-1}$ (40%, 33%, and 10.6%—values not directly shown in Table 2), and the bias by 0.1, 0.1, and $0.02\ Wm^{-2}\ nm^{-1}$ (42%, 40%, and 15%) for the three measured wavelengths, respectively. r increases by 0.13 (19%), 0.07 (7.6%), and at 490 remains the same. Therefore, according to the present data, the best agreement is achieved using the $b_{bp}(700)$ vertical profile with the a_{NAP} model suggested by Babin et al. (2003), that is, the $a_{NAP_Babin_b_{bp}}$ model.

Similarly to NAP simulations, CDOM absorption models were also compared considering three aspects: the Case 1 versus alternative parameterizations, Chl ($a_{CDOM_Case1_Chl}$) versus fDOM IOP depth variability ($a_{CDOM_Case1_fDOM}$), and additional spectral corrections due to modifications in the pure water spectrum shown in Equation 15. As in a_{NAP} , considering shapes alternative to Chl, such as profiles of fDOM, reveals a drastic improvement in the match-up statistics. fDOM-shaped Case 1 model from Morel and Gentili (2009) ($a_{CDOM_Case1_fDOM}$) introduces a RMSE decrease 0.07, 0.07, and $0.02\ Wm^{-2}\ nm^{-1}$ (26.9%, 26.9%, and 11.0%) and a reduction of bias amounting to 0.07, 0.08, and $0.03\ Wm^{-2}\ nm^{-1}$ (38.9%, 44.4%, and 25%). r increases by 0.09, 0.05, and 0.01 (13.2%, 6.3%, and 1.1%), Figure 2c and Table 2. As in Figure 2b, the significant impact on the lowering of bias and RMSE values was also due to a deviation from Case 1 models. This was achieved by adopting the approach presented in Organelli and Claustre (2019), described in Section 2.3.3, with the difference that the first optical depth range was rather considered as it resulted in a better performance compared to the MLD (not shown). Relative to the fDOM-shaped Case 1 model ($a_{CDOM_Case1_fDOM}$), in $a_{CDOM_K_{bio}_Morel}$ the RMSE decreases by 0.05, 0.03, and $0.01\ Wm^{-2}\ nm^{-1}$ (26.3%, 15.8%, and 6.3%) at 380, 412, and 490 nm, respectively. Subsequent simulations result in an upgrade in the calculation of K_w : from the original value of $0.0151\ m^{-1}$ (Morel & Maritorena, 2001), K_w was calculated by taking into consideration the T - S corrections for both absorption and scattering values ($a_{CDOM_K_{bio}_Mason}$). Moreover, the a_{CDOM} was modified for the spectral correction of a_w ($a_{CDOM_K_{bio}_Mason_a_w_corr}$). Compared to the constant K_w value simulation ($a_{CDOM_K_{bio}_Morel}$), the final configuration resulted in a decrease in RMSE by 0.05, 0.04, and $0.03\ Wm^{-2}\ nm^{-1}$ (35.7%, 25.0%, and 6.7%) and in a bias decrease by 0.04, 0.04, and $0.02\ Wm^{-2}\ nm^{-1}$ (44%, 40%, and 20.0%) at 380, 412, and 490 nm, respectively (not directly shown in Table 2).

The contribution of remaining IOPs, phytoplankton absorption a_ϕ and scattering by particles b_p , are shown alongside the skill of the chosen models for separate IOP groups described above, Figure 2d and Table 2. The PFT modeling configuration described in Section 2.3.4, compared to the pure water simulation results, resulted in a RMSE decrease by 0.14, 0.18, and $0.06\ Wm^{-2}\ nm^{-1}$ (32.6%, 41.9%, and 28.6%) and in a bias decrease by 0.15, 0.19, and $0.07\ Wm^{-2}\ nm^{-1}$ (37.5%, 50%, and 43.8%). The correlation increased by 0.23, 0.15, and 0.04 (52.3%, 22.7%, and 4.5%). Based on the phytoplankton absorption curves adopted in the model, the highest decrease in RMSE and bias at 412 nm can be explained by the proximity to the chlorophyll a absorption peak in the blue, which can also explain a more uniform spectral change of skill. Moreover, the absorption values of most PFTs (except *Cryptophytes* and *Synechococcus*) are similar at 380 and 490 nm, with slightly higher values at 380 nm.

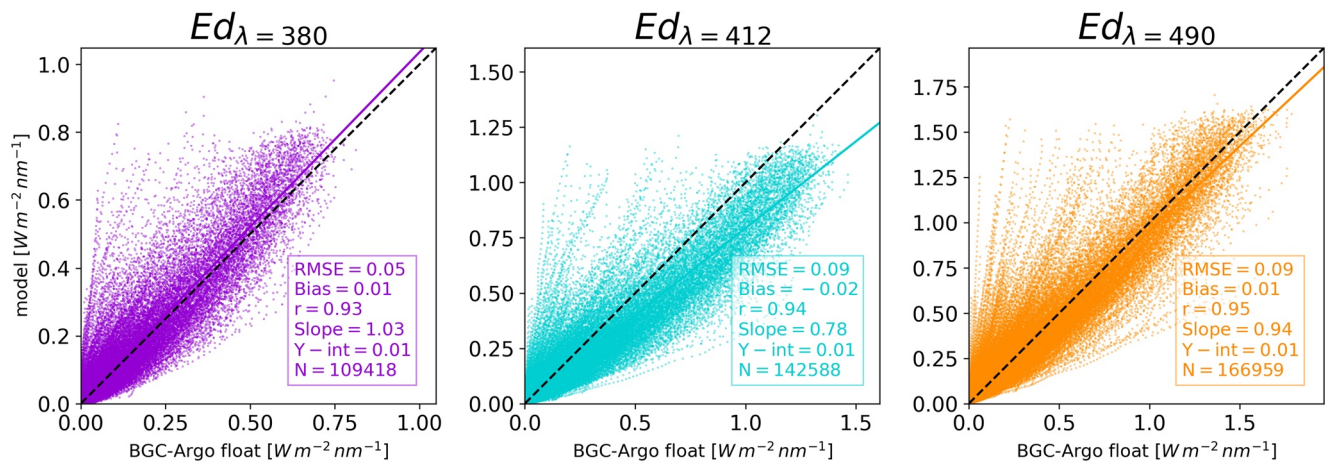


Figure 3. Match-up $E_d(\lambda)$ with the final modeling configuration including all IOPs in the first 150 m, displaying the root mean square error (RMSE), bias, Pearson correlation coefficient (r), slope, intercept (Y -int), and number of points (N) for each of the three wavelengths considered.

Even though several b_p configurations were tested, their impact on the E_d match-up was negligible, leading to small differences between simulation results. The chosen scattering model was a non-Case 1 type derived from $b_{bp}(700)$ measurements following Equations 20 and 21, with a maximum backscattering ratio \tilde{b}_{bp} of 0.015 and a spectral slope η of 3. The selection of these values is motivated by examining K_d and R_{rs} climatologies as discussed in Section 3.2.

The final modeling configuration, including all optically significant constituents considered in this study, that is

$$a_w_Mason + b_w + a_{NAP_Babin_b_{bp}} + a_{CDOM_K_{bio_Mason_a_w_corr}} + a_\phi + b_{p_from_b_{bp}},$$

results in a RMSE ranging from 0.05 to 0.09 $W m^{-2} nm^{-1}$, a negative bias of $-0.02 W m^{-2} nm^{-1}$ at 412 nm and positive values of $0.01 W m^{-2} nm^{-1}$ at 380 and 490 nm, while r is 0.93 at 380 nm, 0.94 at 412 nm, and 0.95 at 490 nm. Figure 3. The slope is closest to 1 at 490 nm, with the highest value observed at 380 nm (1.03), signifying a model overestimation, and lowest slope at 412 nm (0.78), with model values lower than float measurements.

Examples of the model results for west and east are displayed in Figures 4a and 4b, respectively. The top row shows model forcings that were used for IOP parameterization and their depth variability (Chl, $b_{bp}(700)$ and fDOM), whereas the bottom row displays both the model output and radiometric measurements (E_d). Modeled and measured irradiance values are quite in agreement, both in terms of vertical shapes and the first optical (e-folding) depth ranges at all three wavelengths considered. As the model is configured in such way that it takes the IOP depth variability based on the local float biogeochemical measurements, no regional bias was observed in the results. This is quite encouraging given the fact that two different bio-optical regimes are clearly at play in the Western and Eastern Mediterranean. More specifically, the Western Mediterranean subsurface Chl maximum overlaps with the shape of $b_{bp}(700)$, which might suggest that the modifications in Chl are related to actual changes in phytoplankton biomass and community structure, Figure 4a (Barbieux et al., 2018). On the contrary, no such co-variance is observed for the Eastern Mediterranean, and values of $b_{bp}(700)$ are much higher, which might be explained more due to physiology and photoadaptation than to changes in the actual biomass, Figure 4b (Barbieux et al., 2018). Moreover, in the Eastern Mediterranean the particles might be also of more mineral origin due to episodic dust deposition events (Claustre et al., 2002). Such findings clearly demonstrate the importance of having synoptic biogeochemical, bio-optical and radiometric measurements in order to validate the IOP metrics with available irradiance profiles. Furthermore, simulations show that the inclusion of additional parameters (i.e., fDOM and $b_{bp}(700)$) in the IOP parameterizations results in a significant improvement of the match-up statistics compared to Chl-shaped (Case 1) IOP models.

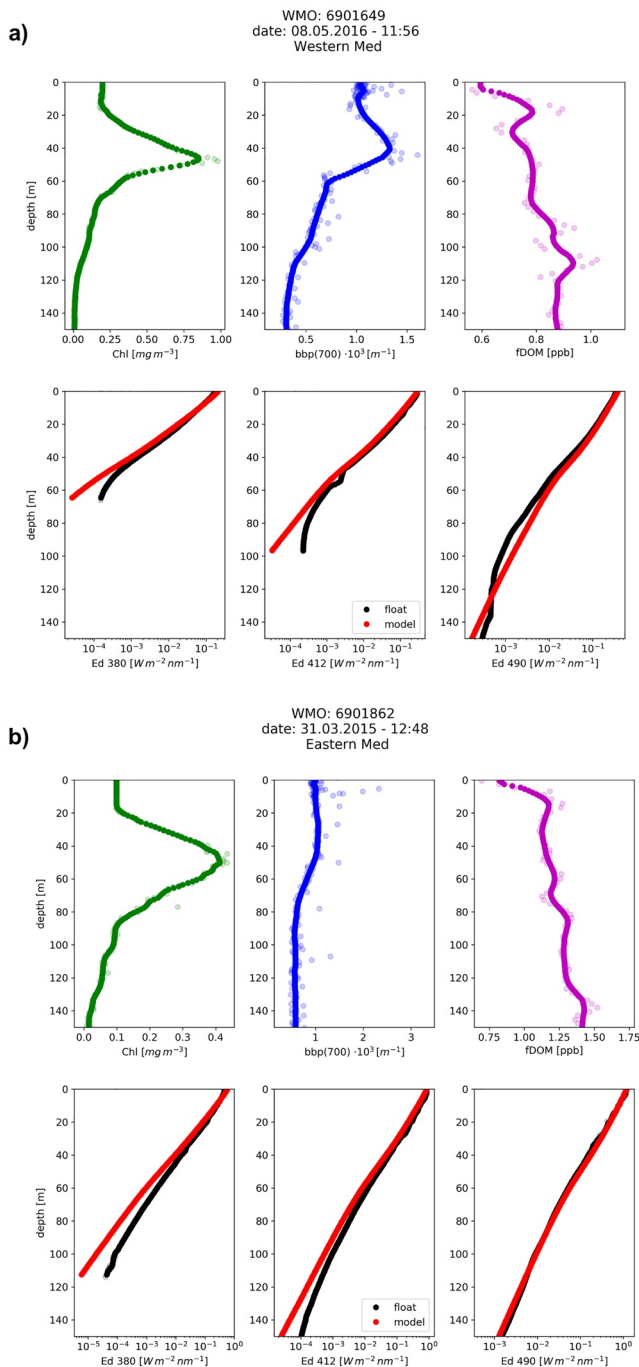


Figure 4. Example of a BGC-Argo profile with modeled and measured radiometric values. Pale dots are values prior to the QC additionally applied to this study. (a) Western Mediterranean. (b) Eastern Mediterranean.

3.2. Comparison With In Situ and Remote Sensing Apparent Optical Properties

Results were further assessed also in terms of diffuse attenuation coefficients for downwelling irradiance $K_d(\lambda)$ and remote sensing reflectance $R_{rs}(\lambda)$. Both AOPs were calculated for the first optical (i.e., e-folding) depth range, following methods described in Sections 2.3 and 2.4. Additionally, for the wavelength 490 nm, a three-platform comparison was possible with model- and float-derived $K_d(490)$ versus satellite data. The match-up of satellite and float observations amounted to 445 co-located measurements which were spatio-temporally aggregated into climatological months and grouped according to western and eastern basins. More information on the number of profiles per month per region is shown in Table 3.

Seasonal Taylor diagrams of $K_d(\lambda)$, divided in west (darker points) and east (lighter points), for RMSE and r values are shown in Figure 5. The aim was to assess the impact of changing the relative contribution of a_{CDOM} within the K_{bio} term as described in Section 2.3.3. The K_{bio} factor was plotted for the extreme ranges of tested values: $f = 0.5$ (opaque) and $f = 1$ (transparent). In terms of the scattering modeling configurations, there was no difference in the skill between the two ranges of backscattering ratio, hence only $\widehat{b_{pp}} = 0.015$ is shown in Figure 5. Different values of slopes are displayed with different markers. Results convey two distinct clusters for the western and eastern basins, which could imply regionally different bio-optical regimes, with RMSE values always lower for the Eastern Mediterranean. Such findings are in line with Terzić et al. (2019), which also shows zonal gradients in modeled and float-derived $K_d(\lambda)$ values. Moreover, changing η values does not seem to have a strong impact on the skill in terms of $K_d(\lambda)$ statistics, as points are in most cases concentrated. K_{bio} factor proves to have the largest impact on the model skill ($f = 0.5$), especially at shorter wavelengths during winter, when RMSE is reduced for more than a factor of 5 at 380 nm. Even though $f = 0.5$ worsens the model match-up in terms of $E_d(a_{CDOM} - 0.5K_{bio} - Mason_{a_w} - corr)$, as shown in Figure 2c and Table 2, this might suggest that optically active constituents absorbing in the UV/blue (such as CDOM) are more important at greater depths, as $K_d(\lambda)$ is assessed only at the first optical depth. This might in turn explain why $f = 1$ works better at greater depths, where fDOM most likely has a larger impact.

Modeled $K_d(\lambda)$ coefficients replicated the monthly dynamics computed from float measurements, Figure 6. At 380 nm, maximum discrepancy is seen in winter and spring months for western basins, with a largest difference in the month of April, with mean values of 0.125 and 0.11 m^{-1} for model and data, respectively (top figure in Figure 6). At longer wavelengths the difference diminishes, with good consistency achieved also between the three comparing platforms at 490 nm. However, satellites do not seem to capture highest values in spring for the Western Mediterranean, which is shown from BGC-Argo floats and model results. Overall, $K_d(\lambda)$ values are larger for western than eastern basins, as shown in Terzić et al. (2019). Modeling IOPs as functions of available biogeochemical

and bio-optical measurements therefore provides a significant reproduction of the zonal gradients. The similar magnitude of error bars from all platforms demonstrates also that the model and data variabilities are close.

Table 3
Number of Matched-Up Profiles per Month per Region (i.e., Western and Eastern Mediterranean)

month	West	East
1	58	42
2	49	48
3	86	69
4	58	70
5	75	110
6	43	48
7	32	38
8	19	26
9	22	16
10	17	22
11	31	25
12	70	42

Considering another AOP, however, a different result is obtained. $R_{rs}(\lambda)$ is related to IOPs in such way that is directly proportional to backscattering and inversely proportional to the sum of absorption and backscattering (Morel & Gentili, 1993; Morel & Prieur, 1977). Raman scattering was accounted for by correcting $R_{rs}(\lambda)$ values according to Lee et al. (2013), and its inclusion amounts to 3.5%, 4%, and 8.5% difference in terms of $R_{rs}(\lambda)$ at 412, 443, and 490, respectively (not shown).

Seasonal Taylor diagrams of $R_{rs}(\lambda)$, divided in west (darker points) and east (lighter points), for RMSE and r values are shown in Figure 7. Unlike in Figure 5, no zonal gradients are observed, instead, points seem to be quite dispersed. r is generally less than 0.6 during most seasons, with exceptions seen in autumn (at 443 nm) and winter (at 490 nm), up to a maximum of around 0.8 and 0.7, respectively. In terms of the K_{bio} factor ($f = 0.5$ displayed as opaque and $f = 1$ as transparent), the greatest impact is seen at higher slope values ($\eta = 4$), for which RMSE decreases at all seasons and wavelengths, however still having highest values among all η . As in Figure 5, changing the K_{bio} factor has a greater impact than changing the backscattering ratio, as the range of tested values is quite small (between 0.2% and 1.5%), and thus only values of $\widehat{b}_{bp} = 0.015$ are shown in Figure 7.

Given the lack of in situ upwelling radiometric measurements, as well as the uncertainty of remote sensing in the blue part of the spectrum, no definite conclusions can be placed on the most adequate scattering model parameters. However, using Case 1 from Equation 19 leads to an underestimation of modeled $R_{rs}(\lambda)$ for both west and east, resulting in up to a 60% discrepancy with satellite values, even when using the $b_{bp}(700)$ shape, and especially during summer months (not shown). By rather focusing on the $b_{bp}(700)$ -derived scattering models while looking at monthly climatological $R_{rs}(\lambda)$ data shown in Figures 8a and 8b, certain range of slope values can be preferred for certain seasons and regions. Lower values ($\eta = 1$) seemed to work best during winter/early spring in the Western Mediterranean (seen from Figure 7), with $\eta = 2$ for the spring in the Eastern Mediterranean, as well as for late spring and summer at west, Figure 8a. $\eta = 3$ resulted in a better agreement with remote-sensing data for summer and autumn in the Eastern Mediterranean, Figure 8b. Slopes of 2 and 3 are also consistent with the range of values from Antoine et al. (2011). This finding might suggest that there are different scattering regimes at play in the two basins, most likely stemming from a different particle size distribution (Antoine et al., 2011), which can provide information also on the dominant phytoplankton (Kostadinov et al., 2009; Organelli et al., 2020). Lower slope values thus imply larger particles, which is consistent with the results in the west during usual spring bloom events with larger, microphytoplankton assemblages (20–200 μm). On the other hand, higher slope values could suggest smaller particles, consistent with the pico- or nanophytoplankton (0.2–2 and 2–20 μm , respectively) assemblages usually predominant at the basin level, with the former prevailing especially during spring/summer and the latter during winter. Such conclusions are in line with the previously detected patterns of phytoplankton distribution in Siokou-Frangou et al. (2010) and Uitz et al. (2012), which were confirmed also by Sammartino et al. (2015), Di Cicco et al. (2017), and Navarro et al. (2017).

4. Conclusions

BGC-Argo floats prove to be an essential observing system to further explore the possibility of integrating data in numerical modeling of physical, as well as biogeochemical and optical properties. Due to the high number of profiles with synoptic measurements of physical and bio-optical parameters, it is possible to use the almost complete suite of measured variables (T , S , Chl , $f\text{DOM}$, $b_{bp}(700)$, and $E_d(\lambda)$) to test various state-of-the-art parameterizations of absorption and scattering properties of sea water constituents. The current wavelength selection of $E_d(\lambda)$ measurements constitutes an ideal tool to explore the part of the spectrum that is least understood, mostly for the contributions from CDOM and NAP. This is particularly true in the Mediterranean Sea, where the blue-to-green reflectance ratio-based algorithms are known to have low performances (Morel & Gentili, 2009) because of the higher-than-expected contribution of CDOM for a given

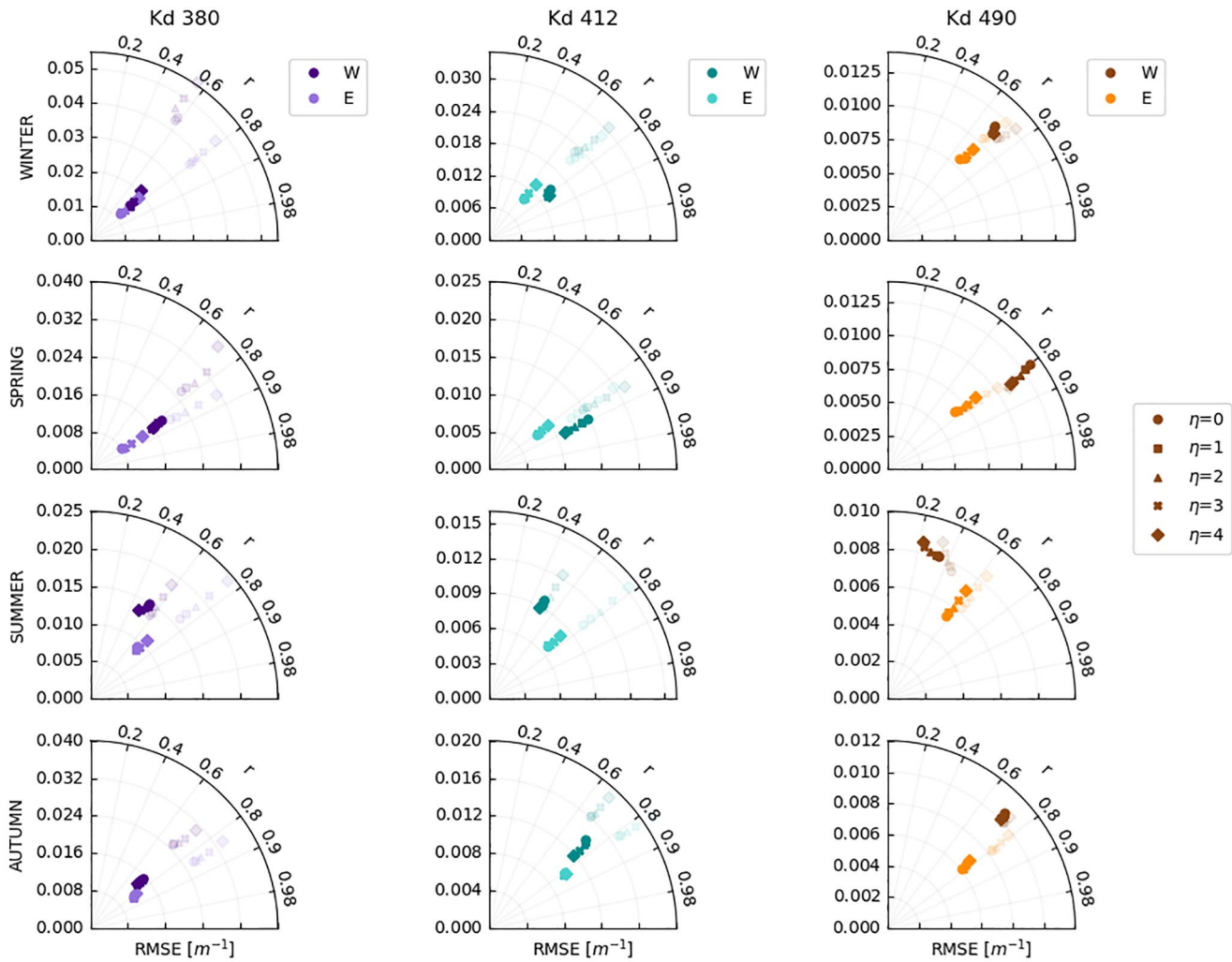


Figure 5. Taylor diagrams of seasonally divided (rows) values of RMSE of $K_d(\lambda)$ at 380, 412, and 490 nm (columns). Dark colors represent the Western Mediterranean, while lighter colors depict the Eastern Mediterranean. Transparent points indicate values of K_{bio} multiplied by a factor f of 1 and the opaque ones stand for a factor of 0.5. The symbols show different values of the slope η .

Chl concentration. The major findings of this work can be summarized as follows: the inclusion of T and S data is recommended to account for the small, but significant spectral modulation of seawater compared to pure water, which also improves the model skill. Furthermore, the tests performed on Case 1 IOP models reveal that the inclusion of additional biogeochemical measurements in the IOP parameterizations results in improved match-up statistics, both when comparing with irradiance profiles, as well as with in situ and remote-sensing derived AOPs. The shape of $b_{bp}(700)$ for a_{NAP} variability increases the skill compared to Chl-shaped models by up to 40% in the case of RMSE. Moreover, it was demonstrated that the use of fDOM shape and the estimation of $a_{CDOM}(380)$ for CDOM absorption from $K_d(380)$, as well as the spectral correction of the updated a_w spectrum, all contribute to an upgrade in CDOM modeling of up to 57.7% in terms of RMSE. Different relative contributions of $K_{bio}(380)$ as an indicator of $a_{CDOM}(380)$ were shown for different metrics, matching up E_d values at a 150 m depth range versus K_d at the first optical depth. Results implied a lower relative contribution of $K_{bio}(380)$ to $a_{CDOM}(380)$ ($f = 0.5$) at shallower depths, and a higher one ($f = 1$) at greater depths, suggesting a major importance of CDOM dynamics also at depths which cannot be captured by satellites. Therefore, partitioning the contributions of NAP and CDOM to the total absorption with additional experiments would be also advantageous, as well as the assessment of relative contributions of different constituents to the total $b_{bp}(700)$ signal, thus separating the organic and inorganic parts.

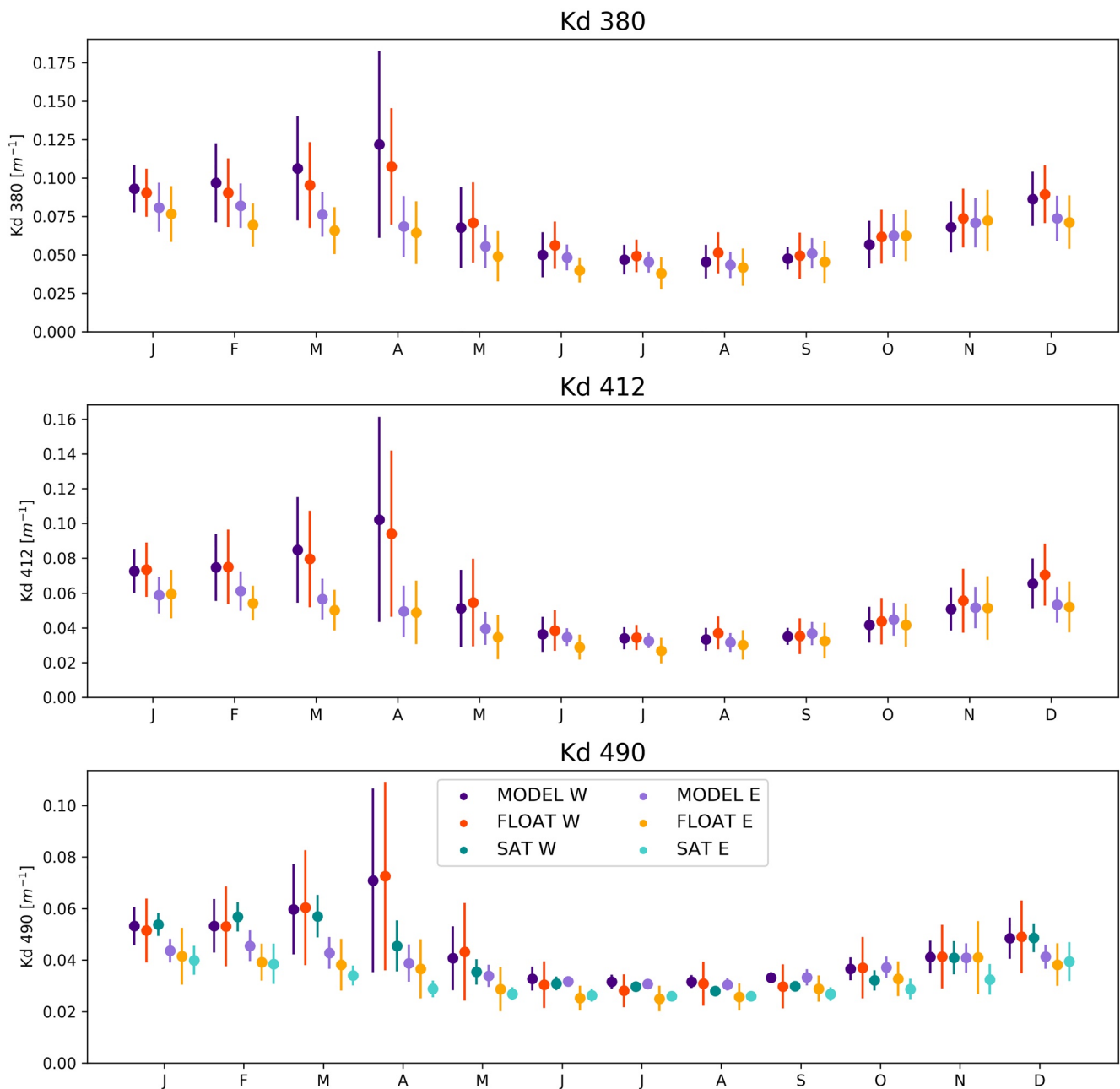


Figure 6. Monthly climatology of $K_d(\lambda)$ values with $a_{CDOM}(380) = f K_{bio}(380)$, where $f = 0.5$. The top two figures display model (purple points) and float (orange points) values for western (darker color) and eastern (lighter color) basins. At 490 nm, additional green scatter points from satellite data are included (bottom figure).

The inclusion of PFTs has demonstrated the importance of accounting also for phytoplankton, resulting in a more uniform spectral response in the blue, decreasing the RMSE up to 41.9% compared to the pure water simulations. Observations of other biogeochemical parameters, such as oxygen, nitrate, and pH, can be possibly integrated with a coupled biogeochemical model. All of these variables are already available on the BGC-Argo float standard configuration (Claustre et al., 2020). This could offer the opportunity, with an existing validation data set, to consider also the phytoplankton ecology and dynamics of separate functional groups. Such work demonstrates the advantages of combining data with numerical models, which can pave way to a better understanding of biogeochemical processes in the examined regions.

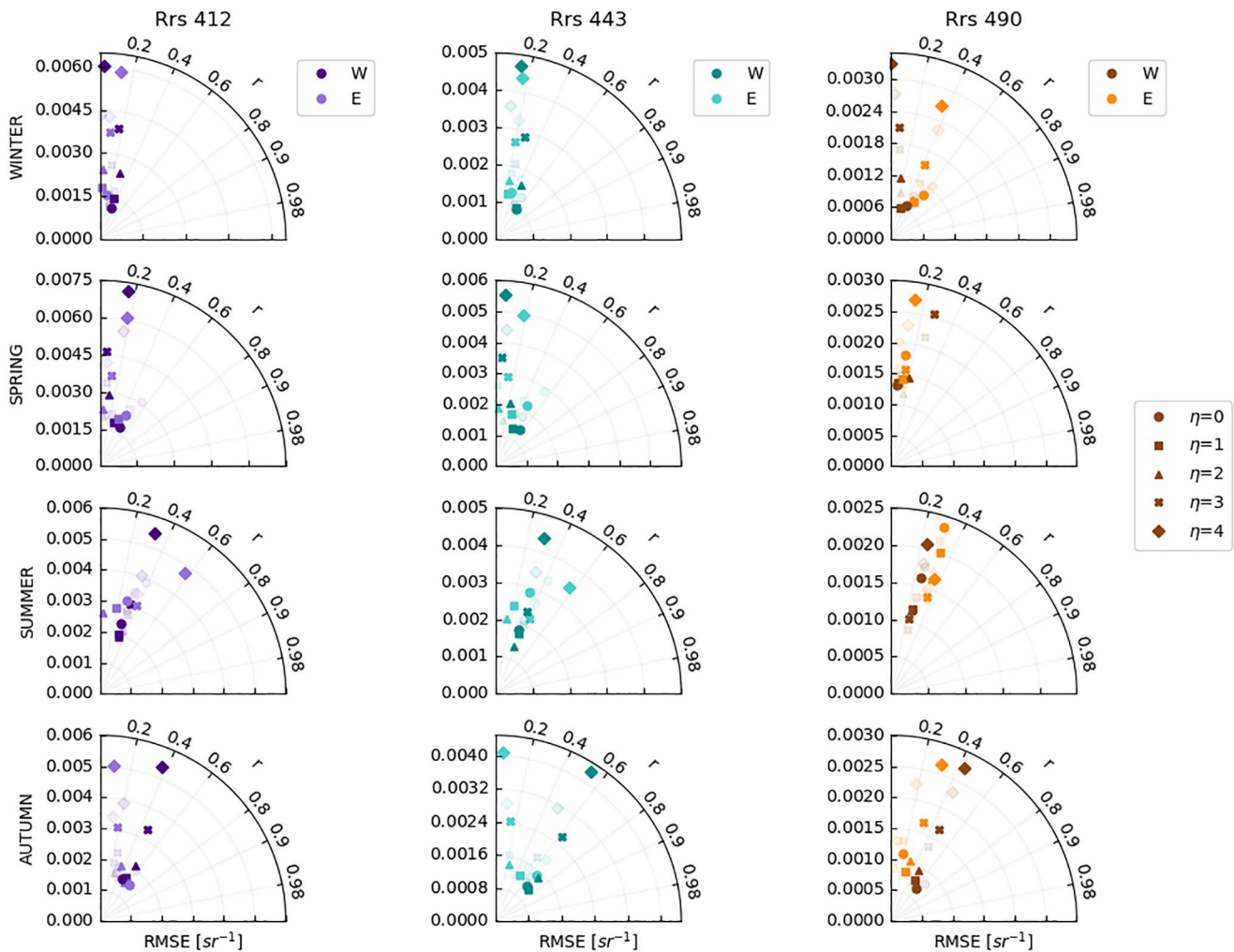


Figure 7. Taylor diagrams of seasonally divided (rows) values of RMSE of $R_{rs}(\lambda)$ at 412, 443, and 490 nm (columns). Dark colors represent the Western Mediterranean, while lighter colors depict the Eastern Mediterranean. Transparent points indicate values of K_{bio} multiplied by a factor f of 1 and the opaque ones stand for a factor of 0.5. The symbols show different values of the slope η .

The focus of this study is also more on the absorption models rather than scattering due to the lack of E_u measurements and the uncertainty of remote sensing in the blue part of the spectrum. However, despite these limitations, the model is still able to capture the spatio-temporal variability of slope values, indicating different phytoplankton and particle size distributions. With the integration of multi-spectral data from platforms like ProVal (Leymarie et al., 2018), it will be possible to further examine this issue in more detail. This will enable also the calculation of in situ R and remote-sensing reflectance estimations R_{rs} , thus surpassing the current limitation of quantifying the skill between R_{rs} satellite data with model values due to the scarcity of satellite observations spatio-temporally co-located with BGC-Argo float profiles, supporting further the three-platform comparisons.

To conclude, the key point raised in this study is that the inclusion of multi-spectral measurements is essential to tackle the proper biogeochemical response, surpassing the most-commonly PAR-related parameterizations of phytoplankton growth. With the advancement of satellite sensors and their algorithms it would be necessary to make a comparison of radiative transfer models of different degrees of complexity, and perform similar tests with hyperspectral models which are able to solve a full radiative transfer equation resulting in a complete radiance distribution (Hedley et al., 2020).

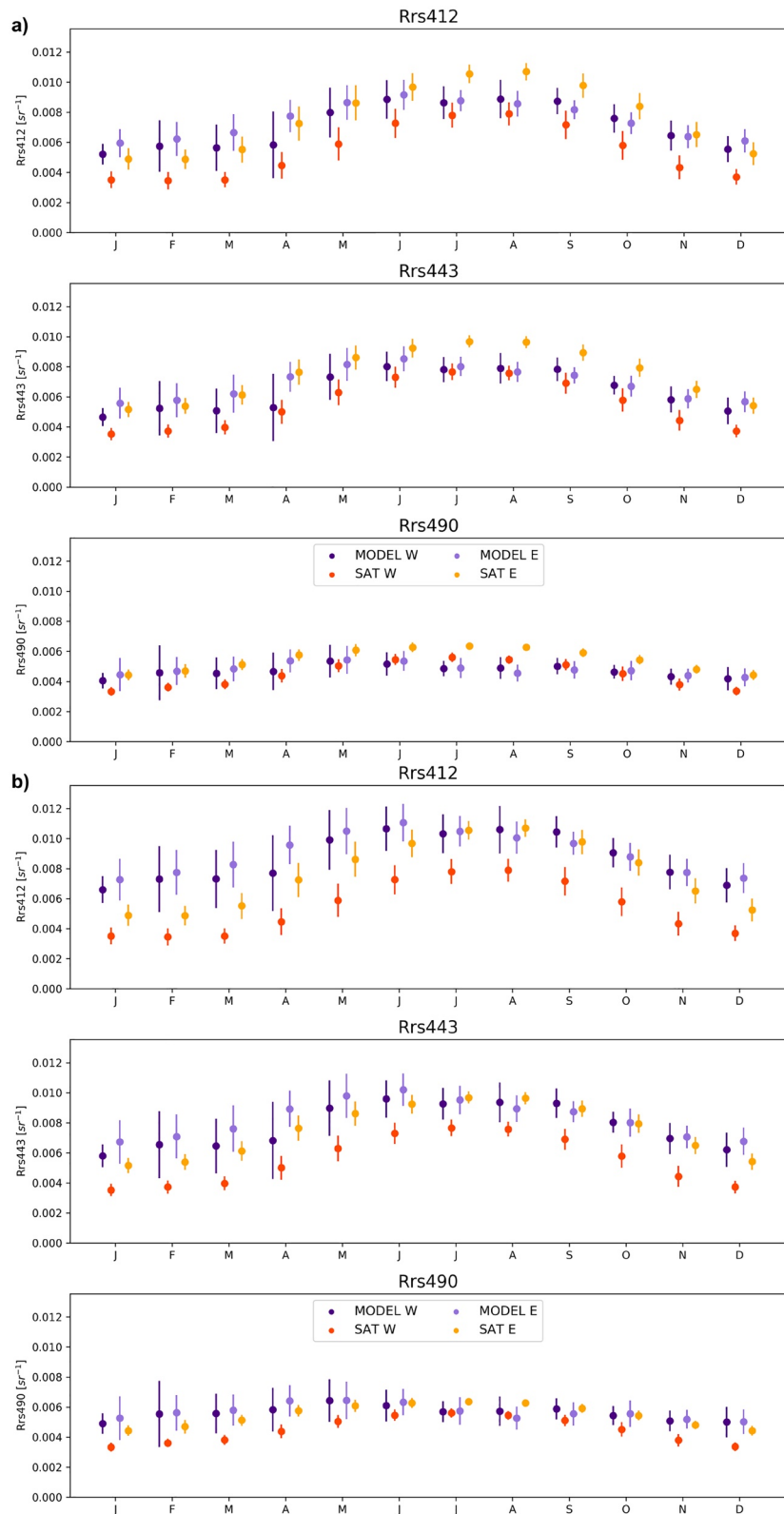


Figure 8. Monthly climatology of $R_{rs}(\lambda)$ values with $a_{CDOM}(380) = fK_{bio}(380)$. All three figures display model (purple points) and satellite (orange points) values for western (darker color) and eastern (lighter color) basins at 412, 443, and 490 nm, respectively. (a) Where $f = 0.5$ and $\eta = 2$. (b) Where $f = 0.5$ and $\eta = 3$.

Data Availability Statement

Data supporting the conclusions are freely available at <https://doi.org/10.17882/42182> without the additional quality control procedures.

Acknowledgments

This work was performed within the framework of the BIOPTIMOD CMEMS Service Evolution project. CMEMS is implemented by Mercator Ocean International within the framework of a delegation agreement with the European Union. This study was supported by the following research projects funding BGC-Argo floats: NAOS (funded by the Agence Nationale de la Recherche in the frame of the French “Equipement d’avenir” program, grant agreement ANR J11R107-F), remOcean (funded by the European Research Council grant agreement 246777), Argo-Italy (funded by the Italian Ministry of Education, University and Research), and the French Bio-Argo program (Bio-Argo France; funded by CNES-TOSCA, LEFE Cyber, and GMMC). The authors would especially like to thank Giorgio Bolzon for his invaluable help and IT support in data management, as well as development of codes and libraries to analyze float and satellite products. Special thanks also to Ilya Chernov (Russian Academy of Science) for his contribution in developing the RT model.

References

- Aas, E. (1987). Two-stream irradiance model for deep waters. *Applied Optics*, 26(11), 2095–2101.
- Antoine, D., Siegel, D. A., Kostadinov, T., Maritorena, S., Nelson, N. B., Gentili, B., et al. (2011). Variability in optical particle backscattering in contrasting bio-optical oceanic regimes. *Limnology & Oceanography*, 56(3), 955–973. <https://doi.org/10.4319/lo.2011.56.3.0955>
- Babin, M., Stramski, D., Ferrari, G. M., Claustre, H., Bricaud, A., Obolensky, G., & Hoepffner, N. (2003). Variations in the light absorption coefficients of phytoplankton, nonalgal particles, and dissolved organic matter in coastal waters around Europe. *Journal of Geophysical Research: Oceans*, 108(C7). <https://doi.org/10.1029/2001jc000882>
- Barbieux, M., Uitz, J., Bricaud, A., Organelli, E., Poteau, A., Schmechtig, C., et al. (2018). Assessing the variability in the relationship between the particulate backscattering coefficient and the chlorophyll a concentration from a global Biogeochemical-Argo database. *Journal of Geophysical Research: Oceans*, 123(2), 1229–1250. <https://doi.org/10.1002/2017jc013030>
- Bellacicco, M., Cornec, M., Organelli, E., Brewin, R. J. W., Neukermans, G., Volpe, G., et al. (2019). Global variability of optical backscattering by non-algal particles from a Biogeochemical-Argo data set. *Geophysical Research Letters*, 46(16), 9767–9776. <https://doi.org/10.1029/2019GL084078>
- Boss, E., Twardowski, M. S., & Herring, S. (2001). Shape of the particulate beam attenuation spectrum and its inversion to obtain the shape of the particulate size distribution. *Applied Optics*, 40(27), 4885–4893. <https://doi.org/10.1364/ao.40.004885>
- Bricaud, A., Babin, M., Claustre, H., Ras, J., & Tièche, F. (2010). Light absorption properties and absorption budget of southeast Pacific waters. *Journal of Geophysical Research: Oceans*, 115(C8). <https://doi.org/10.1029/2009jc005517>
- Bricaud, A., Bosc, E., & Antoine, D. (2002). Algal biomass and sea surface temperature in the Mediterranean basin: Intercomparison of data from various satellite sensors, and implications for primary production estimates. *Remote Sensing of Environment*, 81(2–3), 163–178. [https://doi.org/10.1016/S0034-4257\(01\)00335-2](https://doi.org/10.1016/S0034-4257(01)00335-2)
- Briggs, N., Perry, M. J., Cetinić, I., Lee, C., D’Asaro, E., Gray, A. M., & Rehm, E. (2011). High-resolution observations of aggregate flux during a sub-polar north Atlantic spring bloom. *Deep Sea Research Part I: Oceanographic Research Papers*, 58(10), 1031–1039. <https://doi.org/10.1016/j.dsr.2011.07.007>
- Christaki, U., Giannakourou, A., Van Wambeke, F., & Grégori, G. (2001). Nanoflagellate predation on auto-and heterotrophic picoplankton in the oligotrophic Mediterranean Sea. *Journal of Plankton Research*, 23(11), 1297–1310. <https://doi.org/10.1093/plankt/23.11.1297>
- Claustre, H., Johnson, K. S., & Takeshita, Y. (2020). Observing the global ocean with Biogeochemical-Argo. *Annual Review of Marine Science*, 12, 23–48. <https://doi.org/10.1146/annurev-marine-010419-010956>
- Claustre, H., Morel, A., Hooker, S., Babin, M., Antoine, D., Oubelkheir, K., et al. (2002). Is desert dust making oligotrophic waters greener? *Geophysical Research Letters*, 29(10). <https://doi.org/10.1029/2001gl014056>
- Corsini, G., Grasso, R., & Cipollini, P. (2002). Regional bio-optical algorithms for the Alboran Sea from a reflectance model and in situ data. *Geophysical Research Letters*, 29(15). <https://doi.org/10.1029/2001gl013861>
- Cullen, J. J. (2015). Subsurface chlorophyll maximum layers: Enduring enigma or mystery solved? *Annual Review of Marine Science*, 7(1), 207–239. <https://doi.org/10.1146/annurev-marine-010213-135111>
- de Boyer Montégut, C., Madec, G., Fischer, A. S., Lazar, A., & Iudicone, D. (2004). Mixed layer depth over the global ocean: An examination of profile data and a profile-based climatology. *Journal of Geophysical Research*, 109(C12). <https://doi.org/10.1029/2004jc002378>
- Di Cicco, A., Sammartino, M., Marullo, S., & Santoleri, R. (2017). Regional empirical algorithms for an improved identification of phytoplankton functional types and size classes in the Mediterranean Sea using satellite data. *Frontiers in Marine Science*, 4, 126. <https://doi.org/10.3389/fmars.2017.00126>
- D’Ortenzio, F., Marullo, S., Ragni, M., d’Alcalá, M. R., & Santoleri, R. (2002). Validation of empirical SeaWiFS algorithms for chlorophyll-a retrieval in the Mediterranean Sea: A case study for oligotrophic seas. *Remote Sensing of Environment*, 82(1), 79–94.
- Dutkiewicz, S., Hickman, A. E., Jahn, O., Gregg, W. W., Mouw, C. B., & Follows, M. J. (2015). Capturing optically important constituents and properties in a marine biogeochemical and ecosystem model. *Biogeosciences*, 12(14), 4447–4481. <https://doi.org/10.5194/bg-12-4447-2015>
- Fujii, M., Boss, E., & Chai, F. (2007). The value of adding optics to ecosystem models: A case study. *Biogeosciences*, 4(5), 817–835. <https://doi.org/10.5194/bg-4-817-2007>
- Gitelson, A., Karnieli, A., Goldman, N., Yacobi, Y., & Mayo, M. (1996). Chlorophyll estimation in the Southeastern Mediterranean using CZCS images: Adaptation of an algorithm and its validation. *Journal of Marine Systems*, 9(3–4), 283–290. [https://doi.org/10.1016/S0924-7963\(95\)00047-X](https://doi.org/10.1016/S0924-7963(95)00047-X)
- Gordon, H. R. (1989). Can the Lambert-Beer law be applied to the diffuse attenuation coefficient of ocean water? *Limnology & Oceanography*, 34(8), 1389–1409. <https://doi.org/10.4319/lo.1989.34.8.1389>
- Gregg, W. W., & Casey, N. W. (2009). Skill assessment of a spectral ocean-atmosphere radiative model. *Journal of Marine Systems*, 76(1–2), 49–63. <https://doi.org/10.1016/j.jmarsys.2008.05.007>
- Gregg, W. W., & Rousseaux, C. S. (2016). Directional and spectral irradiance in ocean models: Effects on simulated global phytoplankton, nutrients, and primary production. *Frontiers in Marine Science*, 3, 240. <https://doi.org/10.3389/fmars.2016.00240>
- Gregg, W. W., & Rousseaux, C. S. (2017). Simulating pace global ocean radiances. *Frontiers in Marine Science*, 4, 60. <https://doi.org/10.3389/fmars.2017.00060>
- Hedley, J., Mobley, C. D., & Sundman, L. K. (2020). *HydroLight 6 ecotlight 6*. Retrieved from <https://www.numopt.com/hydroLight.html>
- IOCCG. (2011). *Bio-optical sensors on Argo floats*. IOCCG.
- Kostadinov, T., Siegel, D., & Maritorena, S. (2009). Retrieval of the particle size distribution from satellite ocean color observations. *Journal of Geophysical Research: Oceans*, 114(C9). <https://doi.org/10.1029/2009jc005303>
- Lazzari, P., Salon, S., Terzić, E., Gregg, W. W., D’Ortenzio, F., Vellucci, V., et al. (2021). Assessment of the spectral downward irradiance at the surface of the Mediterranean Sea using the radiative ocean-atmosphere spectral irradiance model (OASIM). *Ocean Science*, 17(3), 675–697. <https://doi.org/10.5194/os-17-675-2021>

- Lee, Z., Carder, K. L., & Arnone, R. A. (2002). Deriving inherent optical properties from water color: A multiband quasi-analytical algorithm for optically deep waters. *Applied Optics*, 41(27), 5755. <https://doi.org/10.1364/AO.41.005755>
- Lee, Z., & Hu, C. (2006). Global distribution of case-1 waters: An analysis from SeaWiFS measurements. *Remote Sensing of Environment*, 101(2), 270–276. <https://doi.org/10.1016/j.rse.2005.11.008>
- Lee, Z., Hu, C., Shang, S., Du, K., Lewis, M., Arnone, R., & Brewin, R. (2013). Penetration of UV-visible solar radiation in the global oceans. *Journal of Geophysical Research: Oceans*, 118(9), 4241–4255. <https://doi.org/10.1002/jgrc.20308>
- Lee, Z., Wei, J., Voss, K., Lewis, M., Bricaud, A., & Huot, Y. (2015). Hyperspectral absorption coefficient of “pure” seawater in the range of 350–550 nm inverted from remote sensing reflectance. *Applied Optics*, 54(3), 546–558. <https://doi.org/10.1364/ao.54.000546>
- Leymarie, E., Penkerch, C., Vellucci, V., Lerebourg, C., Antoine, D., Boss, E., et al. (2018). Proval: A new autonomous profiling float for high quality radiometric measurements. *Frontiers in Marine Science*, 5, 437. <https://doi.org/10.3389/fmars.2018.00437>
- Loisel, H., Vantrepotte, V., Norkvist, K., Meriaux, X., Kheireddine, M., Ras, J., et al. (2011). Characterization of the bio-optical anomaly and diurnal variability of particulate matter, as seen from scattering and backscattering coefficients, in ultra-oligotrophic eddies of the Mediterranean Sea. *Biogeosciences*, 8(11), 3295–3317. <https://doi.org/10.5194/bg-8-3295-2011>
- Mason, J. D., Cone, M. T., & Fry, E. S. (2016). Ultraviolet (250–550 nm) absorption spectrum of pure water. *Applied Optics*, 55(25), 7163. <https://doi.org/10.1364/AO.55.007163>
- Mignot, A., Claustre, H., Uitz, J., Poteau, A., d’Ortenzio, F., & Xing, X. (2014). Understanding the seasonal dynamics of phytoplankton biomass and the deep chlorophyll maximum in oligotrophic environments: A Bio-Argo float investigation. *Global Biogeochemical Cycles*, 28(8), 856–876. <https://doi.org/10.1002/2013gb004781>
- Mobley, C. D., Boss, E., & Roesler, C. (2010). *Ocean optics web book*. Retrieved from <http://www.oceanopticsbook.info>
- Mobley, C. D., Chai, F., Xiu, P., & Sundman, L. K. (2015). Impact of improved light calculations on predicted phytoplankton growth and heating in an idealized upwelling-downwelling channel geometry. *Journal of Geophysical Research: Oceans*, 120(2), 875–892. <https://doi.org/10.1002/2014jc010588>
- Mobley, C. D., Stramski, D., Paul Bissett, W., & Boss, E. (2004). Optical modeling of ocean waters: Is the case 1-case 2 classification still useful? *Oceanography*, 17(2), 60–67. <https://doi.org/10.5670/oceanog.2004.48>
- Morel, A., Antoine, D., & Gentili, B. (2002). Bidirectional reflectance of oceanic waters: Accounting for Raman emission and varying particle scattering phase function. *Applied Optics*, 41(30), 6289–6306. <https://doi.org/10.1364/ao.41.006289>
- Morel, A., Claustre, H., Antoine, D., & Gentili, B. (2007). Natural variability of bio-optical properties in case 1 waters: Attenuation and reflectance within the visible and near-UV spectral domains, as observed in south pacific and Mediterranean waters. *Biogeosciences Discussions*, 4(4), 2147–2178. <https://doi.org/10.5194/bg-4-913-2007>
- Morel, A., & Gentili, B. (1993). Diffuse reflectance of oceanic waters. II. Bidirectional aspects. *Applied Optics*, 32(33), 6864–6879. <https://doi.org/10.1364/ao.32.006864>
- Morel, A., & Gentili, B. (2009). The dissolved yellow substance and the shades of blue in the Mediterranean Sea. *Biogeosciences*, 6(11), 2625–2636. <https://doi.org/10.5194/bg-6-2625-2009>
- Morel, A., Gentili, B., Claustre, H., Babin, M., Bricaud, A., Ras, J., & Tièche, F. (2007). Optical properties of the “clearest” natural waters. *Limnology & Oceanography*, 52(1), 217–229. <https://doi.org/10.4319/lo.2007.52.1.0217>
- Morel, A., & Maritorena, S. (2001). Bio-optical properties of oceanic waters: A reappraisal. *Journal of Geophysical Research: Oceans*, 106(C4), 7163–7180. <https://doi.org/10.1029/2000jc000319>
- Morel, A., & Prieur, L. (1977). Analysis of variations in ocean color 1. *Limnology & Oceanography*, 22(4), 709–722. <https://doi.org/10.4319/lo.1977.22.4.0709>
- Navarro, G., Almaraz, P., Caballero, I., Vázquez, Á., & Huertas, I. E. (2017). Reproduction of spatio-temporal patterns of major Mediterranean phytoplankton groups from remote sensing OC-CCI data. *Frontiers in Marine Science*, 4, 246. <https://doi.org/10.3389/fmars.2017.00246>
- Organelli, E., Bricaud, A., Antoine, D., & Matsuoka, A. (2014). Seasonal dynamics of light absorption by chromophoric dissolved organic matter (CDOM) in the NW Mediterranean Sea (Boussole site). *Deep Sea Research Part I: Oceanographic Research Papers*, 91, 72–85. <https://doi.org/10.1016/j.dsr.2014.05.003>
- Organelli, E., Bricaud, A., Gentili, B., Antoine, D., & Vellucci, V. (2016). Retrieval of colored detrital matter (CDM) light absorption coefficients in the Mediterranean Sea using field and satellite ocean color radiometry: Evaluation of bio-optical inversion models. *Remote Sensing of Environment*, 186, 297–310. <https://doi.org/10.1016/j.rse.2016.08.028>
- Organelli, E., & Claustre, H. (2019). Small phytoplankton shapes colored dissolved organic matter dynamics in the north Atlantic subtropical gyre. *Geophysical Research Letters*, 46(21), 12183–12191. <https://doi.org/10.1029/2019gl084699>
- Organelli, E., Claustre, H., Bricaud, A., Barbieux, M., Uitz, J., D’Ortenzio, F., & Dall’Omo, G. (2017). Bio-optical anomalies in the world’s oceans: An investigation on the diffuse attenuation coefficients for downward irradiance derived from biogeochemical Argo float measurements. *Journal of Geophysical Research: Oceans*, 122(5), 3543–3564. <https://doi.org/10.1002/2016jc012629>
- Organelli, E., Claustre, H., Bricaud, A., Schmechtig, C., Poteau, A., Xing, X., et al. (2016). A novel near-real-time quality-control procedure for radiometric profiles measured by bio-Argo floats: Protocols and performances. *Journal of Atmospheric and Oceanic Technology*, 33(5), 937–951. <https://doi.org/10.1175/jtech-d-15-0193.1>
- Organelli, E., Dall’Omo, G., Brewin, R. J. W., Nencioli, F., & Tarran, G. A. (2020). Drivers of spectral optical scattering by particles in the upper 500 m of the Atlantic Ocean. *Optics Express*, 28(23), 34147–34166. <https://doi.org/10.1364/OE.408439>
- Organelli, E., Nuccio, C., Lazzara, L., Uitz, J., Bricaud, A., & Massi, L. (2017). On the discrimination of multiple phytoplankton groups from light absorption spectra of assemblages with mixed taxonomic composition and variable light conditions. *Applied Optics*, 56(14), 3952. <https://doi.org/10.1364/AO.56.003952>
- Pope, R. M., & Fry, E. S. (1997). Absorption spectrum (380–700 nm) of pure water II Integrating cavity measurements. *Applied Optics*, 36(33), 8710. <https://doi.org/10.1364/AO.36.008710>
- Sammartino, M., Di Cicco, A., Marullo, S., & Santoleri, R. (2015). Spatio-temporal variability of micro-, nano- and pico-phytoplankton in the Mediterranean Sea from Satellite Ocean Colour data of SeaWiFS. *Ocean Science*, 11(5), 759–778. <https://doi.org/10.5194/os-11-759-2015>
- Schmechtig, C., Claustre, H., Poteau, A., & D’Ortenzio, F. (2014). *Bio-Argo quality control manual for the chlorophyll-A concentration (version 1)*. IFREMER.
- Schmechtig, C., Poteau, A., Claustre, H., D’Ortenzio, F., Dall’Omo, G., & Boss, E. (2018). *Processing Bio-Argo particle backscattering at the DAC level*. Retrieved from <https://www.oieau.eu/eaudoc/eaudoc/oai/Processing-Bio-Argo-particle-backscattering-DAC-level>
- Siokou-Frangou, I., Christaki, U., Mazzocchi, M. G., Montresor, M., Ribera d’Alcalá, M., Vaqué, D., & Zingone, A. (2010). Plankton in the open Mediterranean Sea: A review. *Biogeosciences*, 7(5), 1543–1586. <https://doi.org/10.5194/bg-7-1543-2010>

- Smith, R. C., & Baker, K. S. (1981). Optical properties of the clearest natural waters (200–800 nm). *Applied Optics*, *20*(2), 177. <https://doi.org/10.1364/AO.20.000177>
- Sullivan, J. M., Twardowski, M. S., Zaneveld, J. R. V., Moore, C. M., Barnard, A. H., Donaghay, P. L., & Rhoades, B. (2006). Hyperspectral temperature and salt dependencies of absorption by water and heavy water in the 400–750 nm spectral range. *Applied Optics*, *45*(21), 5294. <https://doi.org/10.1364/ao.45.005294>
- Terzić, E., Lazzari, P., Organelli, E., Solidoro, C., Salon, S., D'Ortenzio, F., & Conan, P. (2019). Merging bio-optical data from Biogeochemical-Argo floats and models in marine biogeochemistry. *Biogeosciences*, *16*(12), 2527–2542.
- Uitz, J., Stramski, D., Gentili, B., D'Ortenzio, F., & Claustre, H. (2012). Estimates of phytoplankton class-specific and total primary production in the Mediterranean Sea from Satellite Ocean Color observations. *Global Biogeochemical Cycles*, *26*(2). <https://doi.org/10.1029/2011gb004055>
- Van de Hulst, H. C. (1981). *Light scattering by small particles*. Courier Corporation.
- Volpe, G., Santoleri, R., Vellucci, V., d'Alcalà, M. R., Marullo, S., & d'Ortenzio, F. (2007). The colour of the Mediterranean Sea: Global versus regional bio-optical algorithms evaluation and implication for satellite chlorophyll estimates. *Remote Sensing of Environment*, *107*(4), 625–638. <https://doi.org/10.1016/j.rse.2006.10.017>
- Zhang, X., Hu, L., & He, M.-X. (2009). Scattering by pure seawater: Effect of salinity. *Optics Express*, *17*(7), 5698–5710. <https://doi.org/10.1364/oe.17.005698>